Human-caused sea level rise drives 21st-century worldwide water level extremes

Daniel M. Gilford[1]*, Yucheng Lin[2,3,4], Kristina Dahl[1], Andrew Pershing[1], Robert E. Kopp[4,5], Benjamin Strauss[1]

Short Title: Human-caused sea level rise drives global extremes

One sentence summary/Teaser: Human-caused sea level rise drives 58% of extreme water-level exceedance days and has nearly tripled these days since the 1970s.

Affiliations:

[1]Climate Central; Princeton, NJ, 08542, USA

[2]School of Energy and Environment, City University of Hong Kong, Hong Kong, China

[3]CSIRO Environment, Hobart, TAS, Australia

[4]Department of Earth & Planetary Sciences, Rutgers University, Piscataway, NJ, USA

[5]Rutgers Climate & Energy Institute, Rutgers University, New Brunswick, NJ, USA

*Corresponding author. Email: dgilford@climatecentral.org

Abstract: The rate and impacts of sea level rise vary considerably around the world, but the contribution of human-caused climate change to increases in local and regional flood risks has not yet been systematically explored. Because such information is critical to local decision making, legal proceedings, and loss and damage determinations, we quantify human-caused climate change's contributions to sea level rise at worldwide locations using budget-based and semi-empirical model methods. Results show human-caused sea level rise is quantifiable at 97% of 519 tide gauge sites, and is responsible for 58% (44–65%) of the observed daily extreme water level exceedances over 2000–2018. On average, human-caused sea level rise has caused a near-tripling in the number of days with attributable exceedances since the 1970s.

Sea levels have recently risen across the planet in large part due to human activities (*1*). Accelerating sea level rise is increasing the exposure of people, ecosystems, and infrastructure to coastal flooding—a particular concern in densely populated or socioeconomically-vulnerable regions (*1–3*). But to what degree is sea level rise from human-caused climate change responsible for worsening extreme water levels and coastal flood risk around the world?

1. Introduction

Anthropogenic climate forcing has played a dominant role in global mean sea level rise (GMSLR) over the past 125 years (*1, 4*). Sea level rise acceleration in recent decades has been tied to this forcing (*5, 6*), with strong implications for projected sea level rise through and beyond the year 2100 (*7*). Depending on estimation methods and levels of confidence, human-caused climate change has contributed between about 25% and 70% of the observed GMSLR since 1900 and approaching 100% of the observed rise since 1970 (*4, 8–10*). A recent reassessment of glacial contributions (*11*) and modeling analyses from Grinsted et al. (*12*) suggest that total GMSLR attributability could be 90–100% during the 20th century.

The signal of anthropogenic climate change on modern rates of global sea level rise is detectable in proxy sea-level records as far back as the 1860s (*13*). But the rate of relative sea level rise varies from region to region, and the effects of sea level rise—namely increased coastal flood risk—play out at local scales. Substantial increases in the frequency of extreme water levels have been well documented at both global (*14*) and regional scales (*15–17*) with a median global increase in high-tide flooding of 165% between the 1960-1980 and 1995-2014 time periods (*1*). Attempts to attribute local coastal flood events to this anthropogenic change have been limited, though, and the question of how much of the change in coastal flood risk at any given location is attributable to human-caused climate change remains. The answer to this question has implications for communities' ability to plan for future sea level rise and pursue legal action to address the harms they are experiencing.

Of the few studies that have carried out localized sea level rise attribution, Strauss et al. (*18*) showed that human-caused sea level rise in the New York Tri-State area was responsible for 12% (median estimate) of the total flood losses associated with Hurricane Sandy in 2012. Lincke et al. (*19*) attributed most of the changes in local flood *risks* worldwide to changes in socio-economic development, but acknowledged threats have been increasing due to "climate-induced" global sea level rise. Hino et al. (*20*) empirically attributed flooding events in Annapolis, MD. Treu et al. (*21*) produced the first global dataset of attributable coastal water levels assuming observed trends were 100% attributable, but did not explore this assumption, its components, or alternative counterfactuals.

In this study we quantify how historical sea levels and extreme water levels (EWL) at tide gauge locations around the world have changed in response to human emissions since 1900. We consider multiple attribution scenarios and approaches, quantifying the range of possibilities under different counterfactuals depending on a combination of literature-based, modeling, and observational assumptions. Using tide gauge data, we show that human-caused climate change is now responsible for the preponderance of daily EWL exceedances around the world.

2. Results

2.1 Analysis

Building on the methods of Strauss et al. (*18*), we develop estimates of attributable sea level rise at tide gauges around the world (*22*) using two largely independent approaches.

First, we use a budget-based method that draws on the gridded data of Frederikse et al. (*23*; F20) to calculate gridded local sea level changes over the 1900–2018 period from four individual contributing factors: steric changes, which can be decomposed into a global thermal expansion component and a regional steric term; melt from mountain glaciers; and ice loss from the Greenland and Antarctic ice sheets (GrIS and AIS, respectively). We determine three literature-based estimates (low, central, and high) of the fraction of each factor that is attributable to human-caused climate change and apply that fraction to each factor. The attributable fractions are time-varying averages of the lowest, highest, and best estimates over 1900–2018. They each sum to a set of budget-based attributable sea level rise (ASLR) gridded estimates that are interpolated to tide gauge sites. Throughout this study, we report results for 519 locations where tide gauge budgets are approximately closed or bounded over the satellite era. Gauges at which the budget-based estimate is less than the observed tide gauge trend are included in this set, which may result in an underestimation of ASLR. Exceedance count results are reported at a smaller subset of 279 stations where there is sufficient data with high temporal resolution to compute analyses over at least 1970–2018. Full analysis details are found in Materials and Methods (section 4).

Our second approach for deriving ASLR estimates is semi-empirical (SE). We update the SE model formulation of Kopp et al. (*24*) using Common Era global mean surface temperature (GMST) estimates from (*25*) and GMSLR estimates from (*13*). We then develop two counterfactual scenarios for the period of 1900–2018: 1) a "Stable" scenario, in which historical period GMST is assumed to be near the pre-industrial average; and 2) a CMIP6 (*26*) counterfactual, in which an ensemble of climate models simulate GMST without human greenhouse gas emissions (Fig. S1). We compare the SE-modeled GMSLRs under the Stable counterfactual with SE-modeled GMSLRs calculated from the Hadley Centre/Climatic Research Unit Temperature version 5 (*27*; HadCRUT5), and likewise compare GMSLR modeled under the CMIP6 counterfactual with each historical simulation in the CMIP6 ensemble. The resulting differences are interpreted as ASLR (Fig. S2). We combine these two ASLR estimates into a single SE-model distribution by sampling from them equally. To localize these results to tide gauge locations, we scale the global semi-empirical ASLR curves by the local budget-based ASLR estimates, assuming the scaled relationship between each location's budget and the total global ASLR (i.e. the spatial fingerprint, from the central budget-based scenario) holds.

To calculate the number of days with attributable EWL exceedances over time, we first tally the number of days an EWL threshold (defined as the upper 2σ level of daily highest tides at tide gauge stations over 2002–2018; similar to ref. *17* but with a different tidal datum) was exceeded at a given gauge, then we subtract the annual ASLR in each year for each scenario from each station's historical record and recompute the number of days with EWL exceedances. This approach makes two assumptions about natural variability: First, that the 2000-2018 period encompasses the full range of tidal amplitudes at all tide gauges. Because the magnitude of natural variability in EWL exceedances varies over both space and time in response to seasonal-to-decadal forcing factors such as the 18.6-year nodal tidal cycle (e.g., *28*) and the El Niño Southern Oscillation (ENSO; e.g., *29*), the 19-year period we have chosen for this portion of the

analysis implicitly incorporates both short- and long-term contributors to natural variability. The second assumption we make is that human-caused climate change is not attributably contributing to long-term changes in drivers of natural variability, such as ENSO or storminess.

2.2 Attributable Sea Level Rise

Both budget-based and SE-model results show that global sea level rise has been dominated by human-caused climate change. Budget-based results show 119 (low scenario) to 194 mm (high scenario) of observed GMSLR is attributable (Fig. 1; Fig. S3), or about 57% (low scenario) to 93% (high scenario) of the median estimate of total GMSLR over 1900–2018 (209 mm; *25*). SE calculations of GMSLR are 69% (45–94%) attributable, with the median falling between the budget-based central and low scenario estimates as of 2018. Our total GMSLR attributability is higher than earlier estimates (*9–10*)—but in line with the more recent estimate of (*12*)—likely because of the strong attributability of glaciers over the study period and included in our budget (*11*).

We find that ASLR is nearly ubiquitous worldwide: Our budget-based approach shows that, as of 2018, some amount of positive attributable sea level rise has occurred at 97% of the 519 stations studied (low scenario). Total ASLR is highest in the South Indian and Pacific Oceans, and lowest in the high northern hemisphere. While we find that there are good matches between the total budget trends and observed sea level trends (particularly during the satellite era), our results suggest not all long-term trends can be considered 100% attributable at each site, an important distinction from the assumptions made by (*21*).

Moreover, the factors controlling the total ASLR vary by region and location (Fig. 2). For example, Greenland is an important contributor to ASLR worldwide, but its positive influence is largest for locations in the south Atlantic and north Pacific regions. Meanwhile, thermal expansion, which accounts for an average of 32% of total attributable sea level rise worldwide, plays the largest *relative* role in the attributable rise around South America and in high northern hemisphere regions (in the near-field of ice sheets and glaciers where attributable sea level *falls* offset the thermosteric rise in the total).

A station-by-station decomposition of the factors contributing to ASLR reveals, for example, that at Charleston, SC, the ASLR has been dominated over time by contributions from mountain glaciers and thermal expansion, with an offsetting smaller influence from the regional steric term (Fig. S4). The budget-based and SE model estimates of ASLR at individual stations are strongly similar in 2018 (Fig. S4–S8). However, the SE estimates have total larger uncertainties than the budget-based method. Differences between the two methodological approaches largely reflect that the timeseries of SE models is capturing the global response to CMIP6 historical temperature changes, which exhibit a documented cool bias in the middle 20th century (*30*) then accelerate in the second half of the 20th century, while the budget-based rise is dominated by glacial and thermosteric influences with their own implicit temperature forcings (which rise more steadily over the period). Nevertheless, the SE models—once scaled by the fingerprint of the budget-based ASLR to produce regional estimates (see methods)—yield additional scenarios with which to test exceedance changes, and these agree well with budget-based results.

A select few high-northern hemisphere stations have experienced historically attributable *falls* in sea level, including Sitka AK, where sea levels are attributably dropping due largely to nearby human-induced glacial melt (Fig. S8). This demonstrates that our multi-method attribution

approach captures both attributable falls and rises in sea level, depending on the contributing processes and period considered.

2.3 Days with Attributable EWL Exceedances

Budget-based and SE model results together make clear that ASLR is already the dominant driver of the number of days with EWL exceedances coastal communities are experiencing in the 21st century. Over the past two decades (2000–2018), central scenario budget-based estimates show that ASLR was responsible for 38 to 50 EWL exceedances per decade at the average site (Fig. 3A). In the same time period and scenario, we find that ASLR was responsible for 60% (57–62%) of EWL all exceedances worldwide (Fig. 3B) and resulted in an average of 4.6 attributable days of EWL exceedances per year (Fig. 4). The percentage of attributability under the central scenario is highest (>90%) at low latitudes, weakens to around 60% in the midlatitude regions, and drops sharply to negative attributability (i.e., attributable decreases in daily EWL exceedances) in portions of the northern high latitudes. Under the high budget-based scenario, some sites experienced as many as 8.9 additional exceedances per year (95th percentile across stations) over 2000-2018. Similar to our global budget-based estimates for the central scenario, our SE-based estimates indicate that 56% (42–63%) of EWL exceedances worldwide over 2010–2018 have been attributable to human-caused sea level rise.

Both the budget-based and SE model-based estimates show that the percentage of global EWL exceedances attributable to climate change has grown since the 1950s (Fig. 3–4). Moreover, attributability per the SE-based method generally falls between the high and central budget-based estimates by the 2010s. However, the SE model-based results show a more gradual upward slope since the 1950s than the budget-based results, which show a more rapid rise in EWL exceedances between the 1990s and the 2000s. These differences in pacing and timing likely reflect the global-temperature driven nature of the SE estimate over time, where a mid-century cooling bias in CMIP6 could be influencing results (Fig. S1; *30*). SE model-based estimates of the fraction of attributable EWL exceedances show a more than tripling over the last four decades, from <15% of exceedances being attributable to human-caused climate change in the 1950s (+1σ) to >45% of exceedances in the 2010s being attributable (-1σ). Using the budget-based central scenario, the average site experienced 2.8x more attributable days in 2000–2018 than during 1970–1989. This increase is also widespread: many places around the world have 5–10x more attributable EWL exceedances in recent decades than they did during 1970–1989, including along the U.S. east coast and in the southeast Pacific.

The growth of the number of attributable EWL exceedances is also evident at the regional level and for individual stations (Fig. S4–S8). EWL exceedances in high-latitude regions have a smaller overall attributability percentage, showing how important the mountain glacial fingerprint is for the overall pattern of human influences. The NW Atlantic, the China/Archipelagic Seas, and the NW Pacific all show a strong increase in their exceedance counts and an increase in their percent attributability over the last 50 years. More than 75% of all EWL exceedances in the Indian Ocean, Mediterranean Sea, SW Pacific since the 1970s have been attributable, and the total number of exceedances continues to grow in those regions.

Ultimately, our two methods combine to show that human-caused climate change is responsible for most likely at least 58% (44–65%) of the total EWL exceedances over the last two decades (2000–2018) at sites studied herein. The number of days with attributable EWL exceedances for the average location has approximately tripled since the 1970s. While the differences between

SE-based and budget-based results highlight how counterfactual choice can lead to different conclusions about how exceedances evolve, the ubiquity of attributable sea level rise is leading to a sharp and pervasive increase in extreme water levels along worldwide coasts this century.

3. Discussion

Previous literature has documented both regional and global increases in the frequency of extreme water levels over the last 50-60 years (*1, 15–17*). Our results show that attributable sea level rise is ubiquitous globally and contributes substantially to the increase in extreme water level exceedances—and, by extension, more frequent coastal flood threats— along coastlines worldwide. With the number and attributability of EWL exceedance days growing steeply over the last 70 years, the fingerprint of climate change on coastal flood risk is both clear and persistent.

The multi-method attribution system employed in this study provides a foundation for putting attributable estimates on observed flooding events. For example, it could be used in real-time to identify whether a particular observed coastal flood event would not have happened without human-caused climate change, and to calculate the attributable flood impacts and damages associated with the event. For instance, Strauss et al. (*18*) showed that just ~100 mm of attributable sea level rise caused more than 8 billion USD of damages during Hurricane Sandy (2012); our work forms the foundation for similar studies in the future. Our approach could also be used to calculate the likelihood of given EWL exceedance events, helping to identify highly impacted regions or patterns worthy of deeper research, particularly in regions with fewer attribution studies (*31*). This information could ultimately provide context for communities experiencing frequent coastal flooding, help decision makers understand present and future risks, and inform legal proceedings as well as loss and damage determinations.

When employing this system to perform attribution studies, several caveats should be kept in mind. For one, differences between budget-based and semi-empirical model results reveal that the assumptions one makes about counterfactual scenarios can affect the structure, timing, and attributability of results. And while the budget-based system is modular, enabling it to be updated as new science becomes available, it can only provide reliable estimates of attributable sea level rise where the local sea level budget has closed or been bound. It could further provide some information if one assumed an unattributable residual term in those places where the budget differs from the observed trend. Lack of reliable long-term observations, vertical land motion, and ocean variability combine to confound closing the budget at many places worldwide. As time goes on and improved station, ocean, and land data becomes available, budget estimates of attribution should become more applicable at more locations. The full role of atmosphere and ocean variability has not been interrogated by this study but could be important for individual station results, particularly where intra- and interdecadal process such as the North Atlantic and El Niño Southern Oscillations are known to exert a strong regional influence on local sea and extreme water levels (*32*) and where changes in storm frequency or intensity may be occurring (*33–34*). In this study, we calculate the number of attributable EWL exceedances in the past, which is possible given that historical tide gauge data captures exceedances over a fixed threshold, where we can subtract the amount of ASLR at each gauge to estimate counterfactual water levels and EWL exceedances. Moreover, we report exceedance statistics in aggregate by decade to smooth out the influence of interannual variability. When attempting to calculate the frequency of EWL exceedances in the future or evaluating total exceedances in any one year,

however, it will be critical to consider the combination of natural variability and future sea level rise (*35–36*). Finally, because extreme water level thresholds are not the same as flood risks and do not have a standard definition around the world, as particular flood thresholds as stations become available (such as those produced by Piecuch et al.; *37*), our system can be interrogated to more accurately and precisely evaluate impacts related to attributability.

As coastal flood risks grow with continued human-induced sea level rise, the methods presented here will enable future studies of sea level-related attribution over the historical record, including during past extreme storm-related flooding events, as well as real-time attribution estimates of extreme water level exceedances going forward.

4. Materials and Methods

4.1 Historical Sea Level Observations and Budget Approach

Global and local sea level changes from individual sea level contributors are taken from the data synthesis of Frederikse et al. (*23*, *and references therein*; hereafter F20). The F20 dataset provides annual mean and standard error timeseries of historical sea level contributions (1900–2018) from each of five environmental components on a 0.5º x 0.5º global grid. These contributors are steric sea-level changes, mass loss from mountain glaciers, land-ice loss from the Greenland and Antarctic ice sheets (GrIS and AIS, respectively), and net changes in natural and human terrestrial water storage (TWS). The steric component may be further decomposed into a set of global and regional components (see below).

We seek the sea level contributions from each component since 1900 as well as the fraction of those components that can be attributed to human-caused climate change. To generate the total sea level budget at each location and for each year, we combine the full set of component mean (with summation) and uncertainty estimates (in quadrature, i.e., using the root-sum-square, assuming their independence over time). Budget and attribution estimates throughout this study are regridded to station locations with a Gaussian distance-weighted interpolation. Analyses are produced and reported for locations where tide gauge budgets are approximately closed or bounded over the satellite era (see below).

4.2 Tide Gauge Data & Analysis Locations

We compute results along global coastlines using hourly water levels and tide gauge locations from the Global Extreme Sea Level Analysis (GESLA) version 3 (*22*). With a comprehensive set of transparent quality control flags and long records, GESLA provides the capacity and reliability needed to assess observed water level changes and exceedances along many global coastlines.

Based on several criteria, we choose sets of coastal GESLA stations/locations at which to perform attribution analyses. First, we require that included stations have a GESLA station with "no obvious issues" in their datum and quality control flags. After removing duplicates and filtering based on budget closure (discussed below), there are 519 remaining stations. Next, we narrow the locations down to several station subsets corresponding progressively to the periods of data each tide gauge record has available. These are stations with at least 100 years of data over 1900–2018 (n=10, narrowly distributed over the U.S. and Europe), with at least 30 years of data over 1957–2018 (n=123, more broadly distributed over the northern hemisphere), and with

at least 10 years of data over 2002–2018 (n=386, approaching worldwide coverage, with noticeable gaps in the central Atlantic and north Indian oceans). We use these analysis sets throughout this study to show and discuss results at coastal locations; results are consistent across the set of quality control metrics considered herein. The spatial coherence of results (Fig. 1) supports producing ASLR estimates worldwide; nonetheless while, accordingly, ASLR values computed in our study are available for analysis at all GESLA locations, one should cautiously interpret results from stations that do not meet quality control criteria. Exceedance counts are tallied over the full subset of stations with sufficient data to produce EWL analyses (i.e. daily data over at least 1970–2018; n=279).

4.3 Closing the Budget

An important assumption of our budgetary approach is that the sea level budget closes (or at least approximately closes) on local scales. Although the budget has been shown to close regionally, it is much more difficult to close the budget rates when validating against observed tide gauge records at individual locations around the world (F20). In particular, a poor understanding of ocean dynamics and a lack of reliable vertical land motion records are two primary reasons for misfits between the sum of budget contributions and local observations (e.g, *38*), especially further back in time. Similar to S21, we compare the local total sea level budget estimated from F20 with the local changes over the satellite era (1993–2018). We calculate the linear trends of the GESLA station and sea-level budget annual sea levels in mm/yr. For direct comparison between the trends and budget, we must account for vertical land motion. At each GESLA site we evaluate satellite-era estimates of vertical land motion (VLM) over 1993–2020 (over the altimetry period, from ref. *39*; we note the slight time difference in periods due to data availability). VLM are available at Permanent Service for Mean Sea Level (PSMSL) sites, which are most often but not always co-located with GESLA stations. In cases where they are co-located, we take the exact VLM at the local site, i.e. VLM(λ, ϕ). In cases where a GESLA site is not co-located with a PSMSL location, we use a Gaussian-distance weighting to estimate from the valid VLM neighbors within 120 km of the GESLA site.

We subtract the rate of VLM from the local budget's rate of sea level change to arrive at estimates of the total rate of change (Fig. S9). We then compare those estimates to the observed rate from the tide gauges, either requiring 1) that the Budget-VLM estimated total rate of change fall within $\pm 1\sigma$ of the observed GESLA trend, or 2) that the Budget-VLM estimated total rate of change be less than the observed GESLA trend (a bound estimate that we note potentially *underestimates* attributable sea level rise). We focus the remainder of our analyses on stations whose budgets meet one of these constraints. 519 total stations meet one of these criteria, and 279 have sufficient data to compute exceedance analyses. Notable stations remaining in our dataset are located along North and South American coastlines, western Europe, some Australian sites, Pacific Islands, and along the China Seas and coastline of Japan.

4.4 Budget-based Attribution

Budget-based attributable fractions for each component of sea level rise are taken following the approach of Strauss et al. (*18*), which relies on literature-derived estimates (see their SI Table 3). We quantify time-varying attributable percentages of each term using the best available literature estimates over the periods the studies describe. In the years before or after the valid periods

defining each factor's known attributability, we estimate fractions rise by 1% per year, representing a gradual ramp up of attributability during the periods with unknown (but likely non-zero) fractions. We then define three attribution scenarios intended to represent the best estimates and likely ranges of attributable fractions reported in the literature. These are the low (-1σ; 17th percentile), central (median), and high (+1σ; 83rd percentile) attribution estimate (counterfactual) scenarios, respectively.

For each component of sea level rise, we integrate its observed contribution to sea level change over space and time since 1900 with the attributable fractions from the low, central, and high scenarios. This approach regionalizes ASLR by taking advantage of the spatial fingerprints of each contributor drawn from the gridded data of F20.

Below we describe the attributable fractions of each component and how each was derived from the available literature.

4.4.1 Antarctic Ice Sheet (AIS)

Historical Antarctic ice sheet contributions to global and regional sea level rise are highly uncertain before satellite monitoring. Mass losses following the removal of buttressing ice shelves (e.g., *40*) have historically competed with gains from increased accumulation (e.g., *41*); accordingly, the well-known SROCC review placed combined best estimates at "small, if any, before the 1990s" (*4*). In light of these uncertainties, and in absence of a comprehensive historical AIS record, Frederikse et al. (23) used a polar motion constraint (*43*) to impose global mean sea level contributions at 0.05 ± 0.04 mm yr^{-1} over 1900–1992. While the Antarctic Ice Sheet is potentially a large contributor to future sea level rise (e.g., *43*), historically these mean AIS changes have contributed less than 5% to the total observed global sea level rise. Combined with this small signal is large climate variability, making bulk Antarctic ice sheet mass balance changes perhaps the most confounding contributor to attribute over the satellite era. (e.g., *44*; their section 3.3.1.6 and references therein). Some studies have shown that climate change influences are unlikely to emerge during the 21st century (*45*), while others have shown that attributability can already be shown with regional (*46*) or probabilistic (*47*) approaches, but not holistically for bulk changes across the continent. While there is some consensus that a portion of the observed western AIS mass loss has been due to external forcing over the satellite era, experts do not agree on how much (*48*). There remains strong evidence that internal variability may have strongly influenced or dominated mass-loss trends since 1979 (*49*). Accordingly we take 0% as our low scenario for the attributable percentage contribution. Likewise, following S21 as an bounding exercise, we assume all observed AIS mass losses since 1979 are anthropogenic, setting the high scenario to 100%. Before the satellite era we impose a ramp up in attributability of 1% per year. Finally, we take the central scenario as the midpoint between the high and low scenarios. We note that while AIS historical changes remain uncertain, high scenario ASLR from Antarctica since 1900 never exceeds 16 mm (<8% of total observed GMSL) at any tide gauge, making it overall a minor historical contributor to regional attributable EWL exceedances.

4.4.2 Greenland Ice Sheet (GrIS)

Greenland's mass loss over the 20th century was substantive and historic (*50–53*) and has accelerated in recent years (*54*). While the attributable fractions of Greenland changes have not

been specifically quantified, Trusel et al. (*55*) showed that there is a distinct climate signal in GrIS runoff beginning in the 1980s and the mass balance began to diverge from natural variability around the same time (*56*). We follow the approach of S21 and interpret these by assuming Greenland trends were 100%, 75%, or 50% attributable (high, central, and low scenarios, respectively) from 1980 onwards, and then linearly ramping attributability at 1% per year beforehand (until at 0%).

4.4.3 Mountain Glaciers

Recent estimates of the attributable fraction of mountain glacier loss range from 85% to 130% for alpine glaciers and up to 180% for larger ice caps since 1850 (*11*). Importantly, Roe et al. (*11*) allows the attributable percentages of glacial loss to exceed 100% since pre-industrial, which arises in their estimates of glacial mass gain in the counterfactual (naturally-forced) world without climate change. Because F20 does not distinguish between glacial types, we assume that the alpine percentage applies across our budget. We take the 20-year running mean of ref. *11* attributable fractions from their synthetic Little Ice Age scenarios with cooling that ends abruptly when anthropogenic forcing begins in ~1850 (low scenario, with fractions that start low and increase over time) or with cooling that continues into the 20th century (high scenario, with fractions that start high and decrease over time). The central scenario is taken as the average of the two, which is a nearly constant ~95% over the analysis period. Our final estimates are a set of time-varying fractions which vary over 85–130% percent attributable during the analysis period. Given the term's relatively large magnitude and attributability, this update has resulted in a substantive upward shift in both the total ASLR and the relative (i.e., fractional) importance of glacial loss to ASLR rise compared with S21.

4.4.4 Steric Changes: Global Thermal Expansion & Regional Changes

Following S21, we define the thermal expansion component of sea level rise as the global mean of the steric component (δ_{steric}) from F20. We separate the globally-uniform changes (i.e. global thermal expansion) and residual regional changes at each GESLA location and year over 1957–2018:

$$\delta_{steric}(yr, \lambda, \phi) = \delta_{global-thermosteric}(yr) + \delta_{regional}(yr, \lambda, \phi)$$

Literature estimates for the attributability of $\delta_{\text{global-thermosteric}}$ are strongly and confidently positive, with Marcos et al. (*57*) showing that 87% ± 7% of the thermosteric rise observed in ocean's upper 700m was influenced human-caused warming (1970–2005; 1σ errors). Likewise, previous studies over the full depth of the ocean have shown that human-caused climate change is responsible for the large observed thermal expansion since the 1950s (F20, *58–59*). Following S21, we take these same attributable percentages setting the high, central, and low scenarios to 94%, 87%, and 80%, respectively, over the known period of change (1970–2005). We assume these taper off before 1970 at 1% per year and a similarly ramp up after 2005 (capped at 100%). We compared our budget-based ASLR time series to those derived from Liu et al. (*6*), and while our estimates are slightly higher than theirs, they are within the ranges of uncertainty, particularly during the 1900-1990 period and the most recent decade (Fig. S10).

After removing the global thermosteric term from the steric factor, the remaining ocean changes have a highly variable spatial structure (Fig. S11). This structure suggests the attributable percentage may vary from location to location, making it difficult to apply our methods uniformly, in the same way used for the previous contributors, to arrive at a self-consistent, global, and robust result. But the relatively small but (sometimes) material magnitude (coastal changes up to 30 mm since 1957) of the regional steric term means that it may still be a concern for the purposes of this study (*60–61*), and it could create uncertainty in local estimates of ASLR.

To quantify the attributability of this uncertain regional term, we first define its long-term change as the longest wavelength mode function from an Ensemble Empirical Mode Decomposition (EEMD) (e.g., *62*). EEMD is a noise-assisted filtering method for modeling a timeseries with a finite set of intrinsic modal functions (IMFs). IMFs are drawn from the data by adding an ensemble of white-noise, producing a model ensemble of timeseries, and then performing empirical modal decomposition on each ensemble member. EEMD is performed at every GESLA station on $\delta_{regional}(yr, \lambda, \phi)$, and the resulting longest wavelength function is a monotonic and smoothly-varying timeseries of ocean regional steric changes since 1957.

There is currently not sufficient evidence from the literature to estimate the precise attributability of the long-term trend in this term (*62*). We therefore approach the attribution as a bounding exercise, as we do with AIS; we assume observed long-term changes are anthropogenic, but their sign of change is unknown, fixing the high scenario to 100% and the low scenario to -100%. We then take the central scenario as the midpoint between the high and low scenarios (0%).

The resulting high scenario attributable ocean regional steric term amounts to between -34% and 17% of the total attributable SLR over GESLA stations (95% CI). Around the world, most stations' regional steric changes for the high scenario are negative, but there are positive changes in the regions around Japan and central North Pacific, the central North Atlantic, and the high Arctic latitudes. By definition, the low scenario has an opposite sign to the high scenario results, and the resulting factor acts as an uncertainty in our final ASLR totals.

4.4.5 Terrestrial-water Storage (TWS)

Since this study's focus is specifically on the components of sea level changes attributable to human emissions, we ignore anthropogenic changes in TWS, setting the attributable percentage to 0% for all scenarios. We note that this implicitly assumes that any anthropogenic precipitation changes are net zero contributors to TWS worldwide; a full analysis including precipitation effects is beyond the scope of this work.

4.5 Semi-empirical (SE) Modeled Sea Levels & Attribution

To complement our budget-based estimates (and following S21), we develop semi-empirical (SE) modeled estimates of ASLR over 1900–2018. Semi-empirical models take advantage of the historical relationship between global mean surface temperature (T) and the rate of GMSLR change ($\frac{dh}{dt}$) during the last two millennia to predict a range of sea level changes as a function of temperature changes (e.g., *64*). In this study, we use the SE model formulation of Kopp et al. (*24,* K16):

$$\frac{dh}{dt} = a(T(t) - T_0(t) + c(t))$$

where a represents the sensitivity of sea level to deviations from the equilibrium temperature $T_0(t)$ and $c(t)$ is a temperature-independent rate term reflecting a small residual trend, arising from the long-term response to earlier climate changes (e.g., deglaciation). More details about this SE model can be found in K16. We update the SE model parameter posterior distributions in K16 using new Common Era GMST estimates from ref. *25* and GMSLR estimates from ref. *13*. The posterior distributions of SE model parameters were sampled using the Metropolis-Hastings algorithm with Markov Chains–-these are thinned to every 100th sample, with the first 1,000 samples discarded during the burn-in period, resulting in 1,000 parameter combinations. The SE model is implemented within the PaleoSTeHM framework, an open-source platform for paleoenvironmental reconstructions (*65*). A comparison of the updated posterior parameter distributions with those from K16 is provided in Table S1.

We employ this semi-empirical model to develop two counterfactuals derived from assumptions about the GMST over the historical period of 1900–2018. These are (1) a "Stable" counterfactual, in which historical period GMST is assumed to be near the pre-industrial average, and (2) a Climate Model Intercomparison Project Phase 6 (*26*) counterfactual, in which an ensemble of climate models simulate GMST without human greenhouse gas emissions (Fig. S1–S2).

To run the Stable simulations we combine the 1,000 posterior parameter distributions from the SE model with 100 HadCRUT5 temperature samples (drawn from an AR(1) process with a 10-year correlation e-folding time) and a single temperature curve from the Stable counterfactual. For each of the 1,000 SE model parameter sets, we compute the difference in GMSLR between each HadCRUT5 temperature sample and the Stable counterfactual. The resulting 100,000 difference timeseries are interpreted as the distribution of global ASLR for the Stable counterfactual.

For the CMIP6-based simulations, all available climate models with both historical (38 models) and natural-forcing-only (11 models with both) experiments are used. We randomly sample 100 temperature curves from the historical and natural-forcing-only experiments with a uniform distribution. These are then combined with the 1,000 SE model parameter sets to generate 100,000 GMSLR curves for each of the historical and natural-forcing-only scenarios. The difference between these GMSLR curves is similarly interpreted as the distribution of global ASLR for the CMIP6 counterfactual.

As the Stable and CMIP6 GMSLR medians are strongly consistent since 1950, we uniformly combine an equal number of samples from each scenario to form a single SE-modeled distribution for further attribution analysis throughout this study. Results are shown in Fig. S2.

Global ASLR curves from semi-empirical models are localized to tide gauge stations following the procedure of S21. We first find the relationship between the budget-based central scenario ASLR and the total global mean ASLR in 2018 at each gauge location, producing a spatially-varying fingerprint of the scale between them. For instance, in Charleston the central ASLR estimate is 144 mm, with a scaling factor of about 0.92 of the central scenario's global mean estimate of ASLR (156 mm). We then multiply these scales by each semi-empirical ASLR timeseries, transforming the global ASLR estimates directly output from the SE models into tide-gauge-local SE-based ASLR estimates.

References

1. V. Eyring, N. P. Gillett, K. M. Achuta Rao, R. Barimalala, M. Barreiro Parrillo, N. Bellouin, C. Cassou, P. J. Durack, Y. Kosaka, S. McGregor, S. Min, O. Morgenstern, Y. Sun, Human influence on the climate system, in Climate Change 2021: The Physical Science Basis. Contribution of Working Group I to the Sixth Assessment Report of the Intergovernmental Panel on Climate Change, V. Masson-Delmotte *et al.*, Eds. (Cambridge Univ. Press, Cambridge, United Kingdom, and New York, NY, USA, 2021), pp. 423–552. https://doi.org/10.1017/9781009157896.005
2. S. Dangendorf, C. C. Hay, F. M. Calafat, M. Marcos, C. G. Piecuch, K. Berk, J. Jensen, Persistent acceleration in global sea-level rise since the 1960s, *Nat. Clim. Change* **9**, 705–710 (2019). https://doi.org/10.1038/s41558-019-0531-8
3. S. A. Kulp, B. H. Strauss, New elevation data triple estimates of global vulnerability to sea-level rise and coastal flooding, *Nat. Commun.* **10**, 4844 (2019). https://doi.org/10.1038/s41467-019-12808-z
4. M. Oppenheimer, B. C. Glavovic, J. Hinkel, R. van de Wal, A. K. Magnan, A. Abd-Elgawad, R. Cai, M. Cifuentes-Jara, R. M. DeConto, T. Ghosh, J. Hay, F. Isla, B. Marzeion, B. Meyssignac, Z. Sebesvari, Sea level rise and implications for low-lying islands, coasts and communities, in IPCC Special Report on the Ocean and Cryosphere in a Changing Climate, H.-O. Portner, D. C. Roberts, V. Masson-Delmotte *et al.* Eds. (Cambridge Univ. Press, Cambridge, United Kingdom, and New York, NY, USA, 2019), pp. 321–446. https://doi.org/10.1017/9781009157964.006
5. A. B. A. Slangen, J. A. Church, X. Zhang, D. P. Monselesan, The sea level response to external forcings in historical simulations of CMIP5 climate models, *J. Climate* **28**, 8521–8539 (2015). https://doi.org/10.1175/JCLI-D-15-0376.1
6. Z. Liu, C. Chen, G. Wang, S. Li, S. Liu, Regional Sea Level Response to External Forcings from the Twentieth to the Twenty-First Century, *J. Climate* **37**, 3237–3248 (2024). https://doi.org/10.1175/JCLI-D-23-0427.1
7. P. U. Clark, J. D. Shakun, S. A. Marcott, A. C. Mix, M. Eby, S. Kulp, A. Levermann, G. A. Milne, P. L. Pfister, B. D. Santer, D. P. Schrag, S. Solomon, T. F. Stocker, B. H. Strauss, A. J. Weaver, R. Winkelmann, D. Archer, E. Bard, A. Goldner, K. Lambeck, R. T. Pierrehumbert, G.-K. Plattner, Consequences of twenty-first-century policy for multi-millennial climate and sea-level change, *Nat. Clim. Change* **6**, 360–369 (2016). https://doi.org/10.1038/nclimate2923
8. M. Becker, M. Karpytchev, S. Lennartz-Sassinek, Long-term sea level trends: Natural or anthropogenic?, *Geophys. Res. Lett.* **41**, 5571–5581 (2014). https://doi.org/10.1002/2014GL061027
9. S. Dangendorf, M. Marcos, A. Muller, E. Zorita, R. Riva, K. Berk, J. Jensen, Detecting anthropogenic footprints in sea level rise, *Nat. Commun.* **6**, 7849 (2015). https://doi.org/10.1038/ncomms8849
10. A. B. A. Slangen, J. A. Church, C. Agosta, X. Fettweis, B. Marzeion, K. Richter, Anthropogenic forcing dominates global mean sea-level rise since 1970, *Nat. Clim. Change* **6**, 701–705 (2016). https://doi.org/10.1038/nclimate2991
11. G. H. Roe, J. E. Christian, B. Marzeion, On the attribution of industrial-era glacier mass loss to anthropogenic climate change, *Cryosphere* **15**, 1889–1905 (2021). https://doi.org/10.5194/tc-15-1889-2021

12. A. Grinsted, J. Bamber, R. Bingham, S. Buzzard, I. Nias, K. Ng, J. Weeks, The transient sea level response to external forcing in CMIP6 models, *Earth's Future* **10**, e2022EF002696 (2022). https://doi.org/10.1029/2022EF002696
13. J. S. Walker, R. E. Kopp, C. M. Little, B. P. Horton, Timing of emergence of modern rates of sea-level rise by 1863, *Nat. Commun.* **13**, 966 (2022). https://doi.org/10.1038/s41467-022-28564-6
14. P. L. Woodworth, D. L. Blackman, Evidence for systematic changes in extreme high waters since the mid-1970s, *J. Climate* **17**, 1190–1197 (2004). https://doi.org/10.1175/1520-0442(2004)017<1190:EFSCIE>2.0.CO;2
15. B. S. Hague, S. McGregor, B. F. Murphy, R. Reef, D. A. Jones, Sea level rise driving increasingly predictable coastal inundation in Sydney, Australia, *Earth's Future* **8**, e2020EF001607 (2020). https://doi.org/10.1029/2020EF001607
16. S. Li, T. Wahl, J. Fang, L. Liu, T. Jiang, High-tide flooding along the China coastline: Past and future, *Earth's Future* **11**, e2022EF003225 (2023). https://doi.org/10.1029/2022EF003225
17. W. Sweet, B. Hamlington, R. E. Kopp, C. Weaver, P. L. Barnard, D. Bekaert, W. Brooks, M. Craghan, G. Dusek, T. Frederikse, G. Garner, A. S. Genz, J. P. Krasting, E. Larour, D. Marcy, J. J. Marra, J. Obeysekera, M. Osler, M. Pendleton, D. Roman, L. Schmied, W. Veatch, K. D. White, C. Zuzak, Global and regional sea level rise scenarios for the United States: Updated mean projections and extreme water level probabilities along U.S. coastlines (NOAA Tech. Rep. NOS 01, National Oceanic and Atmospheric Administration, National Ocean Service, Silver Spring, MD, 2022).
18. B. H. Strauss, P. M. Orton, K. Bittermann, M. K. Buchanan, D. M. Gilford, R. E. Kopp, S. Kulp, C. Massey, H. de Moel, S. Vinogradov, Economic damages from Hurricane Sandy attributable to sea level rise caused by anthropogenic climate change, *Nat. Commun.* **12**, 2720 (2021). https://doi.org/10.1038/s41467-021-22838-1
19. D. Lincke, J. Hinkel, M. Mengel, R. J. Nicholls, Understanding the drivers of coastal flood exposure and risk from 1860 to 2100, *Earth's Future* **10**, e2021EF002584 (2022). https://doi.org/10.1029/2021EF002584
20. M. Hino, S. T. Belanger, C. B. Field, A. R. Davies, K. J. Mach, High-tide flooding disrupts local economic activity, *Sci. Adv.* **5**, eaau2736 (2019). https://doi.org/10.1126/sciadv.aau2736
21. S. Treu, S. Muis, S. Dangendorf, T. Wahl, J. Oelsmann, S. Heinicke, K. Frieler, M. Mengel, Reconstruction of hourly coastal water levels and counterfactuals without sea level rise for impact attribution, *Earth Syst. Sci. Data* **16**, 1121–1136 (2024). https://doi.org/10.5194/essd-16-1121-2024
22. I. D. Haigh, M. Marcos, S. A. Talke, P. L. Woodworth, J. R. Hunter, B. S. Hague, A. Arns, E. Bradshaw, P. Thompson, GESLA Version 3: A major update to the global higher-frequency sea-level dataset, *Geosci. Data J.* **10**, 293–314 (2023). https://doi.org/10.1002/gdj3.174
23. T. Frederikse, F. Landerer, L. Caron, S. Adhikari, D. Parkes, V. W. Humphrey, S. Dangendorf, P. Hogarth, L. Zanna, L. Cheng, The causes of sea-level rise since 1900, *Nature* **584**, 393–397 (2020). https://doi.org/10.1038/s41586-020-2591-3
24. R. E. Kopp, A. C. Kemp, K. Bittermann, B. P. Horton, J. P. Donnelly, W. R. Gehrels, C. C. Hay, J. X. Mitrovica, E. D. Morrow, S. Rahmstorf, Temperature-driven global sea-level variability in the Common Era, *Proc. Natl. Acad. Sci. U.S.A.* **113**, E1434–E1441 (2016). https://doi.org/10.1073/pnas.1517056113

25. PAGES2k Consortium, Consistent multidecadal variability in global temperature reconstructions and simulations over the Common Era, *Nat. Geosci.* **12**, 643–649 (2019). https://doi.org/10.1038/s41561-019-0400-0
26. V. Eyring, S. Bony, G. A. Meehl, C. A. Senior, B. Stevens, R. J. Stouffer, K. E. Taylor, Overview of the Coupled Model Intercomparison Project Phase 6 (CMIP6) experimental design and organization, *Geosci. Model Dev.* **9**, 1937–1958 (2016). https://doi.org/10.5194/gmd-9-1937-2016
27. C. P. Morice, J. J. Kennedy, N. A. Rayner, J. P. Winn, E. Hogan, R. E. Killick, R. J. H. Dunn, T. J. Osborn, P. D. Jones, I. R. Simpson, An updated assessment of near-surface temperature change from 1850: the HadCRUT5 dataset, *J. Geophys. Res. Atmos.* **126**, e2019JD032361 (2021). https://doi.org/10.1029/2019JD032361
28. D. Peng, E. M. Hill, A. J. Meltzner, A. D. Switzer, Tide gauge records show that the 18.61-year nodal tidal cycle can change high water levels by up to 30 cm, *J. Geophys. Res. Oceans* **124**, 736-749 (2019). https://doi.org/10.1029/2018JC014695
29. W. V. Sweet, A. S. Genz, M. Menendez, J. J. Marra, J. Obeysekera, Implications of variability and trends in coastal extreme water levels, *Geophys. Res. Lett.* **51**, e2024GL108864 (2024). https://doi.org/10.1029/2024GL108864
30. C. M. Flynn, T. Mauritsen, On the climate sensitivity and historical warming evolution in recent coupled model ensembles, *Atmos. Chem. Phys.* **20**, 7829–7842 (2020). https://doi.org/10.5194/acp-20-7829-2020
31. F. E. L. Otto, L. Harrington, K. Schmitt, S. Philip, S. Kew, G. J. van Oldenborgh, R. Singh, J. Kimutai, P. Wolski, Challenges to understanding extreme weather changes in lower income countries, *Bull. Am. Meteorol. Soc.* **101**, E1851–E1860 (2020). https://doi.org/10.1175/BAMS-D-19-0317.1
32. D. Stammer, A. Cazenave, R. M. Ponte, M. E. Tamisiea, Causes for contemporary regional sea level changes, *Annu. Rev. Mar. Sci.* **5**, 21–46 (2013). https://doi.org/10.1146/annurev-marine-121211-172406
33. I. D. Haigh, R. J. Nicholls, N. C. Wells, Assessing changes in extreme sea levels: Application to the English Channel, 1900-2006, *Cont. Shelf Res.* **30**, 1042–1055 (2010). https://doi.org/10.1016/j.csr.2010.02.002
34. W. V. Sweet, A. S. Genz, M. Menendez, J. J. Marra, J. Obeysekera, Implications of variability and trends in coastal extreme water levels, *Geophys. Res. Lett.* **51**, e2024GL108864 (2024). https://doi.org/10.1029/2024GL108864
35. J. Hunter, A simple technique for estimating an allowance for uncertain sea-level rise, *Clim. Change* **113**, 239–252 (2012). https://doi.org/10.1007/s10584-011-0332-1
36. S. Vitousek, P. L. Barnard, C. H. Fletcher, N. Frazer, L. Erikson, C. D. Storlazzi, Doubling of coastal flooding frequency within decades due to sea-level rise, *Sci. Rep.* **7**, 1399 (2017). https://doi.org/10.1038/s41598-017-01362-7
37. C. G. Piecuch, S. B. Das, L. Gorrell, S. Dangendorf, B. D. Hamlington, P. R. Thompson, T. Wahl, Impact-based thresholds for investigation of high-tide flooding in the United States, *Earth's Future* **13**, e2024EF005850 (2025). https://doi.org/10.1029/2024EF005850
38. J. Wang, J. A. Church, X. Zhang, J. M. Gregory, L. Zanna, X. Chen, Evaluation of the local sea-level budget at tide gauges since 1958, *Geophys. Res. Lett.* **48**, e2021GL094502 (2021). https://doi.org/10.1029/2021GL094502
39. W. C. Hammond, G. Blewitt, C. Kreemer, R. S. Nerem, GPS imaging of global vertical land motion for studies of sea level rise, *J. Geophys. Res. Solid Earth* **126**, e2021JB022355 (2021). https://doi.org/10.1029/2021JB022355

40. D. G. Vaughan, C. S. M. Doake, Recent atmospheric warming and retreat of ice shelves on the Antarctic Peninsula, *Nature* **379**, 328–331 (1996). https://doi.org/10.1038/379328a0
41. B. Medley, E. R. Thomas, Increased snowfall over the Antarctic Ice Sheet mitigated twentieth-century sea-level rise, *Nat. Clim. Change* **9**, 34–39 (2019). https://doi.org/10.1038/s41558-018-0356-x
42. S. Adhikari, L. Caron, B. Steinberger, J. T. Reager, K. K. Kjeldsen, B. Marzeion, E. Larour, E. R. Ivins, What drives 20th century polar motion?, *Earth Planet. Sci. Lett.* **502**, 126–132 (2018). https://doi.org/10.1016/j.epsl.2018.08.059
43. R. M. DeConto, D. Pollard, R. B. Alley, I. Velicogna, E. Gasson, N. Gomez, S. Sadai, A. Condron, D. M. Gilford, E. L. Ashe, R. E. Kopp, D. Li, A. Dutton, The Paris Climate Agreement and future sea-level rise from Antarctica, *Nature* **593**, 83–89 (2021). https://doi.org/10.1038/s41586-021-03427-0
44. M. Meredith, M. Sommerkorn, S. Cassotta, C. Derksen, A. Ekaykin, A. Hollowed, G. Kofinas, A. Mackintosh, J. Melbourne-Thomas, M. M. C. Muelbert, T. Ottersen, H.-O. Pörtner, E. A. Pakhomov, J. R. Rintoul, Polar regions, in IPCC Special Report on the Ocean and Cryosphere in a Changing Climate, H.-O. Pörtner, *et al.*, Eds. (Cambridge Univ. Press, Cambridge, United Kingdom, and New York, NY, USA, 2019). https://doi.org/10.1017/9781009157964.005
45. D. P. Lowry, M. Krapp, N. R. Golledge, A. Alevropoulos-Borrill, The influence of emissions scenarios on future Antarctic ice loss is unlikely to emerge this century, *Commun. Earth Environ.* **2**, 221 (2021). https://doi.org/10.1038/s43247-021-00289-2
46. J. E. Christian, A. A. Robel, G. Catania, A probabilistic framework for quantifying the role of anthropogenic climate change in marine-terminating glacier retreats, *Cryosphere* **16**, 2725–2743 (2022). https://doi.org/10.5194/tc-16-2725-2022
47. A. T. Bradley, D. T. Bett, P. R. Holland, C. R. Williams, R. J. Arthern, J. De Rydt, A framework for estimating the anthropogenic part of Antarctica's sea level contribution in a synthetic setting, *Commun. Earth Environ.* **5**, 121 (2024). https://doi.org/10.1038/s43247-024-01287-w
48. J. L. Bamber, M. Oppenheimer, R. E. Kopp, W. P. Aspinall, R. M. Cooke, Ice sheet contributions to future sea-level rise from structured expert judgment, *Proc. Natl. Acad. Sci. U.S.A.* **116**, 11195–11200 (2019). https://doi.org/10.1073/pnas.1817205116
49. A. A. Robel, G. H. Roe, M. Haseloff, Response of marine-terminating glaciers to forcing: Time scales, sensitivities, instabilities, and stochastic dynamics, *J. Geophys. Res. Earth Surf.* **123**, 2205–2227 (2018). https://doi.org/10.1029/2018JF004709
50. B. Marzeion, J. G. Cogley, K. Richter, D. Parkes, Attribution of global glacier mass loss to anthropogenic and natural causes, *Science* **345**, 919–921 (2014). https://doi.org/10.1126/science.1254702
51. K. K. Kjeldsen, N. J. Korsgaard, A. A. Bjørk, S. A. Khan, J. E. Box, S. Funder, N. K. Larsen, J. L. Bamber, W. Colgan, M. R. van den Broeke, M.-L. Siggaard-Andersen, C. Nuth, A. Schomacker, C. S. Andresen, E. Willerslev, K. H. Kjær, Spatial and temporal distribution of mass loss from the Greenland Ice Sheet since AD 1900, *Nature* **528**, 396–400 (2015). https://doi.org/10.1038/nature16183
52. M. R. van den Broeke, E. M. Enderlin, I. M. Howat, P. Kuipers Munneke, B. P. Y. Noël, W. J. van de Berg, E. van Meijgaard, B. Wouters, On the recent contribution of the Greenland ice sheet to sea level change, *Cryosphere* **10**, 1933–1946 (2016). https://doi.org/10.5194/tc-10-1933-2016
53. J. L. Carrivick, C. M. Boston, J. L. Sutherland, D. Pearce, H. Armstrong, A. Bjørk, K. K. Kjeldsen, J. Abermann, R. P. Oien, M. Grimes, W. H. M. James, M. W. Smith, Mass loss of

glaciers and ice caps across Greenland since the Little Ice Age, *Geophys. Res. Lett.* **50**, e2023GL103950 (2023). https://doi.org/10.1029/2023GL103950

54. M. Bevis, C. Harig, S. A. Khan, A. Brown, F. J. Simons, M. Willis, X. Fettweis, M. R. van den Broeke, F. B. Madsen, E. Kendrick, D. J. Caccamise II, T. van Dam, P. Knudsen, T. Nylen, Accelerating changes in ice mass within Greenland, and the ice sheet's sensitivity to atmospheric forcing, *Proc. Natl. Acad. Sci. U.S.A.* **116**, 1934–1939 (2019). https://doi.org/10.1073/pnas.1806562116
55. L. D. Trusel, S. B. Das, M. B. Osman, M. J. Evans, B. E. Smith, X. Fettweis, J. R. McConnell, B. P. Y. Noël, M. R. van den Broeke, Nonlinear rise in Greenland runoff in response to post-industrial Arctic warming, *Nature* **564**, 104–108 (2018). https://doi.org/10.1038/s41586-018-0752-4
56. J. Mouginot, E. Rignot, A. A. Bjørk, M. R. van den Broeke, R. Millan, M. Morlighem, B. Noël, B. Scheuchl, M. Wood, Forty-six years of Greenland Ice Sheet mass balance from 1972 to 2018, *Proc. Natl. Acad. Sci. U.S.A.* **116**, 9239–9244 (2019). https://doi.org/10.1073/pnas.1904242116
57. M. Marcos, A. Amores, Quantifying anthropogenic and natural contributions to thermosteric sea level rise, *Geophys. Res. Lett.* **41**, 2502–2507 (2014). https://doi.org/10.1002/2014GL059766
58. A. B. A. Slangen, J. A. Church, X. Zhang, D. Monselesan, Detection and attribution of global mean thermosteric sea level change, *Geophys. Res. Lett.* **41**, 5951–5959 (2014). https://doi.org/10.1002/2014GL061356
59. K. B. Tokarska, G. C. Hegerl, A. P. Schurer, A. Ribes, J. T. Fasullo, Quantifying human contributions to past and future ocean warming and thermosteric sea level rise, *Environ. Res. Lett.* **14**, 074020 (2019). https://doi.org/10.1088/1748-9326/ab23c1
60. A. B. A. Slangen, M. Carson, C. A. Katsman, R. S. W. van de Wal, A. Köhl, L. L. A. Vermeersen, D. Stammer, Projecting twenty-first century regional sea-level changes, *Clim. Change* **124**, 317–332 (2014). https://doi.org/10.1007/s10584-014-1080-9
61. M. P. Couldrey, J. M. Gregory, F. B. Dias, P. Dobrohotoff, C. M. Domingues, O. Garuba, S. M. Griffies, H. Haak, A. Hu, M. Ishii, J. Jungclaus, A. Köhl, S. J. Marsland, S. Ojha, O. A. Saenko, A. Savita, A. Shao, D. Stammer, T. Suzuki, A. Todd, L. Zanna, What causes the spread of model projections of ocean dynamic sea-level change in response to greenhouse gas forcing?, *Clim. Dyn.* **56**, 155–187 (2021). https://doi.org/10.1007/s00382-020-05471-4
62. Z. Wu, N. E. Huang, Ensemble empirical mode decomposition: A noise-assisted data analysis method, *Adv. Adapt. Data Anal.* **1**, 1–41 (2009). https://doi.org/10.1142/S1793536909000047
63. J. T. Fasullo, R. S. Nerem, Altimeter-era emergence of the patterns of forced sea-level rise in climate models and implications for the future, *Proc. Natl. Acad. Sci. U.S.A.* **115**, 12944–12949 (2018). https://doi.org/10.1073/pnas.1813233115
64. S. Rahmstorf, A semi-empirical approach to projecting future sea-level rise, *Science* **315**, 368–370 (2007). https://doi.org/10.1126/science.1135456
65. Y. Lin, R. E. Kopp, A. Reedy, M. Turilli, S. Jha, E. L. Ashe, PaleoSTeHM v1.0: A modern, scalable spatiotemporal hierarchical modeling framework for paleo-environmental data, *Geosci. Model Dev.* **18**, 2609–2637 (2025). https://doi.org/10.5194/gmd-18-2609-2025
66. S. Dangendorf, Q. Sun, T. Wahl, P. Thompson, J. X. Mitrovica, B. Hamlington, Probabilistic reconstruction of sea-level changes and their causes since 1900, *Earth Syst. Sci. Data* **16**, 3471–3494 (2024). https://doi.org/10.5194/essd-16-3471-2024

Acknowledgments: We thank Ben Hague, John Fasullo, and Sonke Dangendorf for helpful discussions which improved this work.

Funding: This work was supported by the Bezos Earth Fund and the National Science Foundation as part of the Megalopolitan Coastal Transformation Hub (MACH) under NSF award ICER-2103754. This is MACH contribution number 52. This work was also supported by NSF Awards 2002437 and 2148265, NASA Grant 80NSSC17K0698, the NASA Sea Level Change Team (JPL task no. 105393.509496.02.08.13.31), and the Australia Climate Service.

Author contributions:

Conceptualization: BS, DMG, KD, REK, YL

Methodology: AP, BS, DMG, KD, REK, YL

Software: DMG, YL

Validation: DMG, YL

Formal Analysis: DMG, YL

Investigation: DMG, YL

Data Curation: DMG, YL

Writing – original draft: DMG

Writing – review & editing: AP, BS, DMG, KD, REK, YL

Visualization: DMG, YL

Supervision: AP, BS, KD

Project administration: BS, KD

Funding acquisition: AP, BS, REK

Competing interests: Authors declare that they have no competing interests.

Data, Code, and Materials Availability: All data and code needed to evaluate and reproduce the results in the paper are present in the paper and/or the Supplementary Materials. This study did not generate new materials. Data and code are publicly available at doi:10.5281/zenodo.15446540 and doi:10.5281/zenodo.18010948.

Supplementary Materials

Figs. S1 to S11

Tables S1

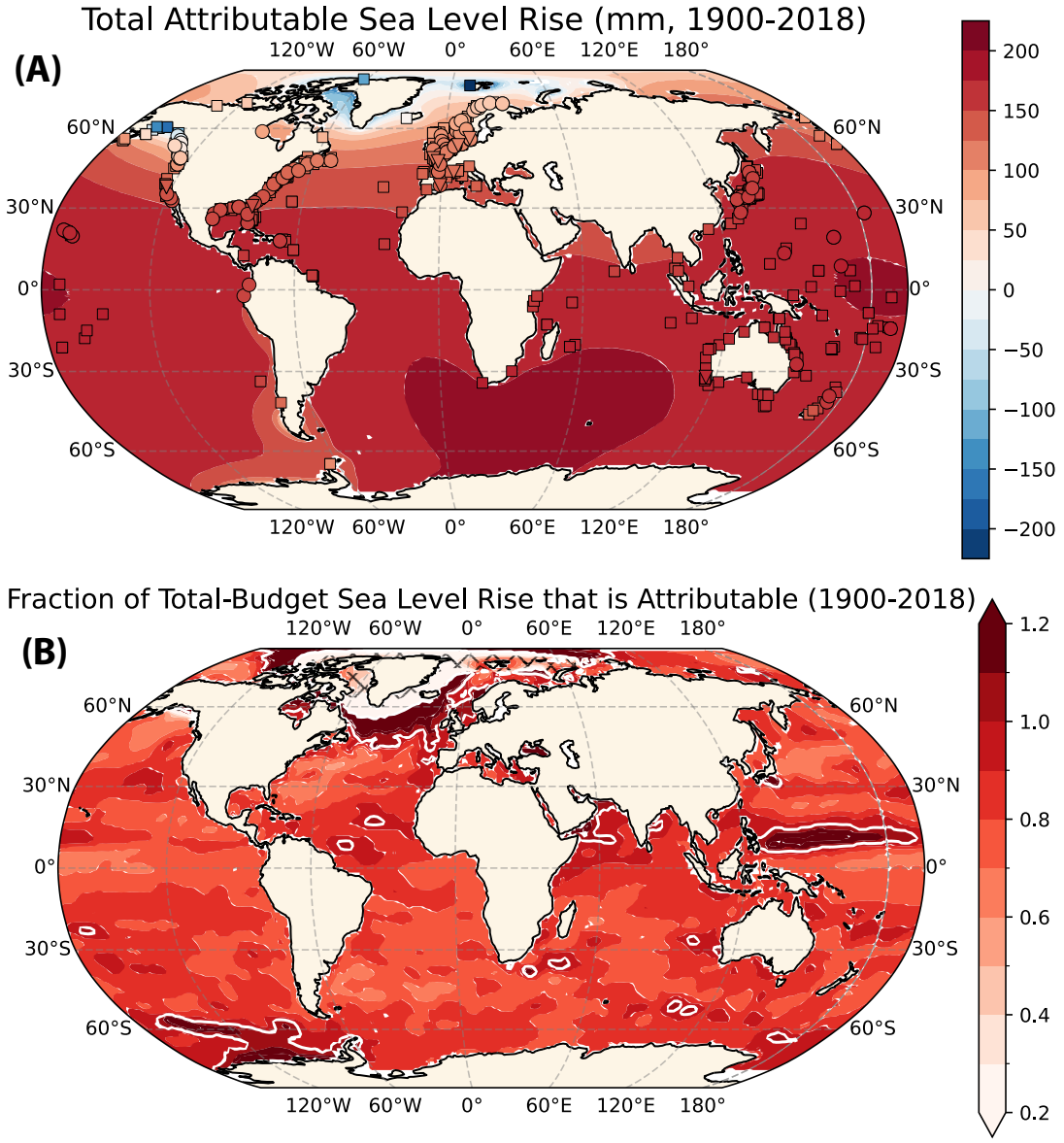

Fig. 1. Worldwide budget-based attributable sea level estimates. (**A**) Total attributable central-scenario estimates of sea level rise (mm) from the budget-based method, gridded worldwide and interpolated to select GESLA stations with closed or bound budgets over 1900–2018. (**B**) Fraction of the gridded total-budgeted sea level rise that is attributable since 1900 (white line is the 1.0 contour). Hatched regions show where the total attributable change (denominator) is negative.

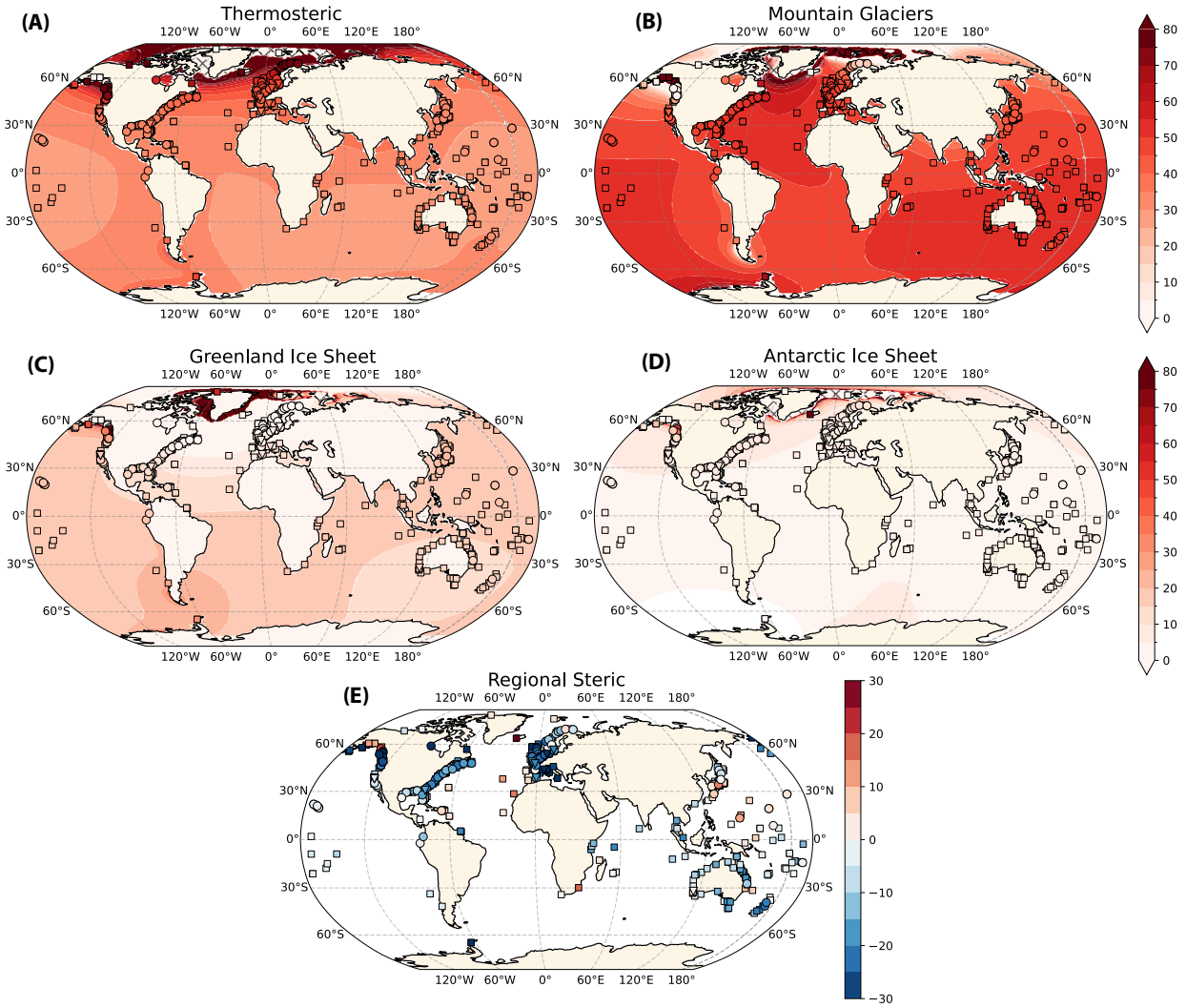

Fig. 2. Percentage of the total budget-based attributable sea level rise accounted for by each contributing factor. Included are Thermosteric (**A**), Mountain Glaciers (**B**), Greenland Ice Sheet (**C**), and Antarctic Ice Sheet (**D**) percentages over 1900–2018. The ocean regional steric factor (**E**, over 1957–2018) can be a positive or negative percentage of the whole (cf. Fig. 1). Hatched regions show where the total attributable change (denominator) is negative. Values are interpolated to select GESLA stations with closed or bound budgets over 1900–2018. Symbols represent select quality-controlled GESLA stations with at least 100 years of data over 1900–2018 (upside-down triangles), with at least 30 years of data over 1957–2018 (circles), and with at least 10 years of data over 2002–2018 (squares).

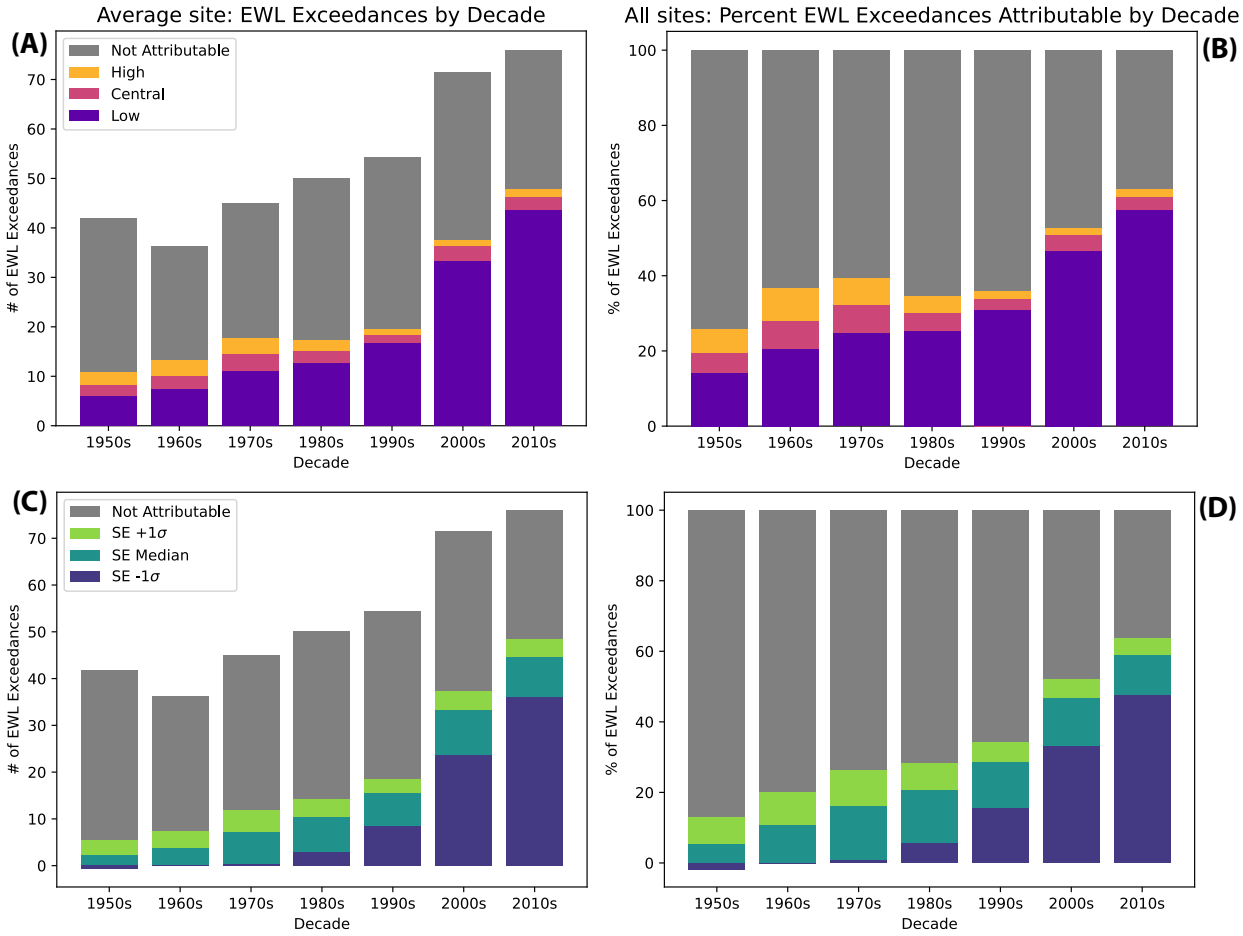

Fig. 3. Attributable extreme water level exceedances grouped by decade across tide gauge stations. (left column, **A, C**) Station-mean cumulative number of decadal non-attributable (grey bars) and attributable (colored bars; associated with each counterfactual) exceedances. (right column, **B, D**) Percentage of total non-attributable (grey bars) and attributable (colored bars) exceedances per decade across all sites. The top row (**A, B**) shows exceedances and percentages associated with budget-based (high, central, low) counterfactuals; the bottom row (**C, D**) shows the 17th, 50th, and 83rd quantiles of the semi-empirical model counterfactual.

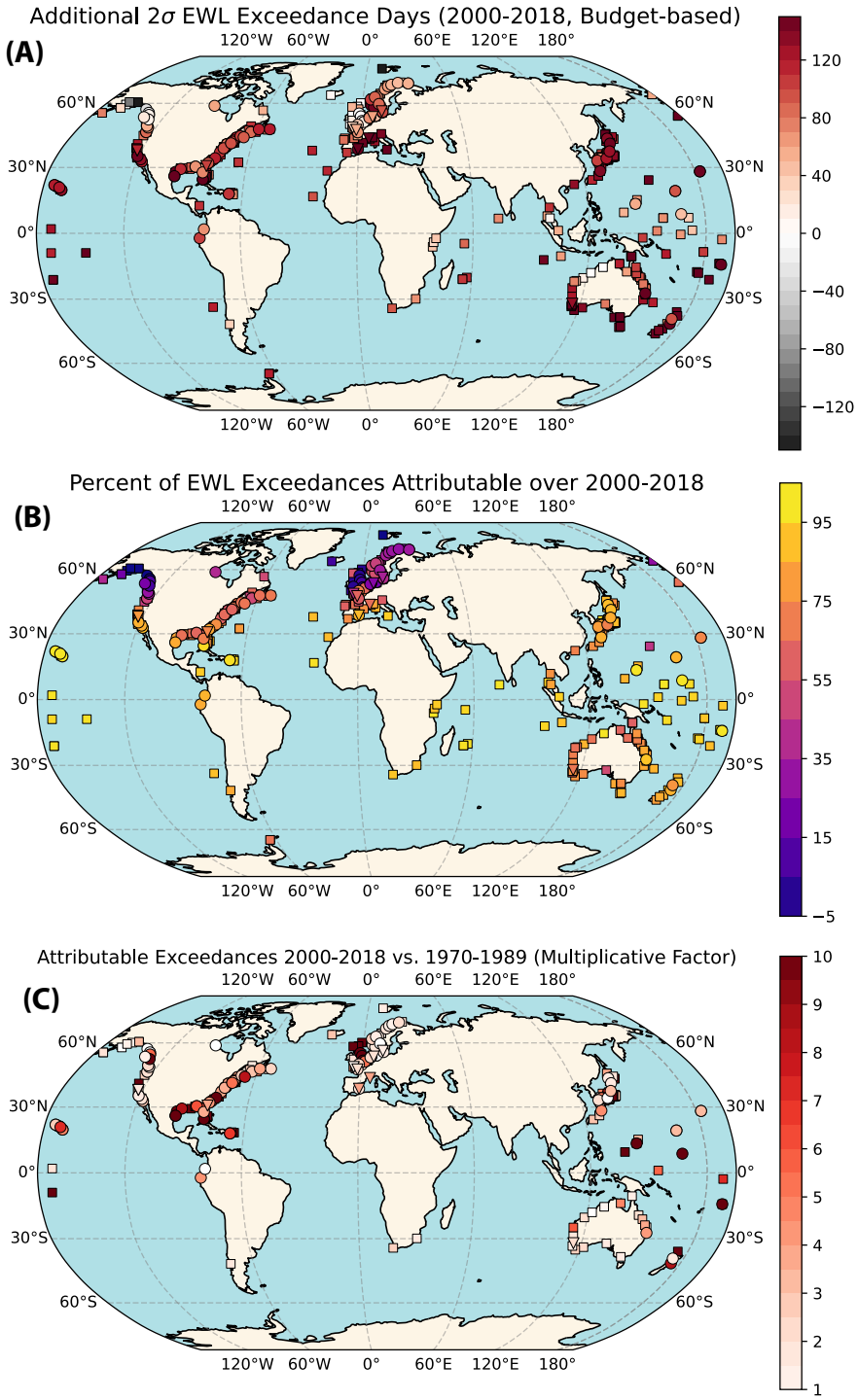

Fig. 4. Worldwide changes in attributable exceedances at tide gauge stations. (**A**) Count of total attributable EWL exceedance days due to human-caused climate change summed over 2000–2018. (**B**) Percentage of the total observed EWL exceedances that were attributable (in **A**) over 2000–2018. (**C**) Ratio of attributable EWL exceedances over 2000–2018 compared to 1970–1989, illustrating the increase in the number of attributable exceedances over time. All computed with the central budget-based counterfactual scenario.

Supplementary Materials for

Human-caused sea level rise drives 21st-century worldwide water level extremes

Daniel M. Gilford, Yucheng Lin, Kristina Dahl, Andrew Pershing, Robert E. Kopp, Benjamin Strauss
Corresponding author: dgilford@climatecentral.org

The PDF file includes:

Figs. S1 to S11
Table S1

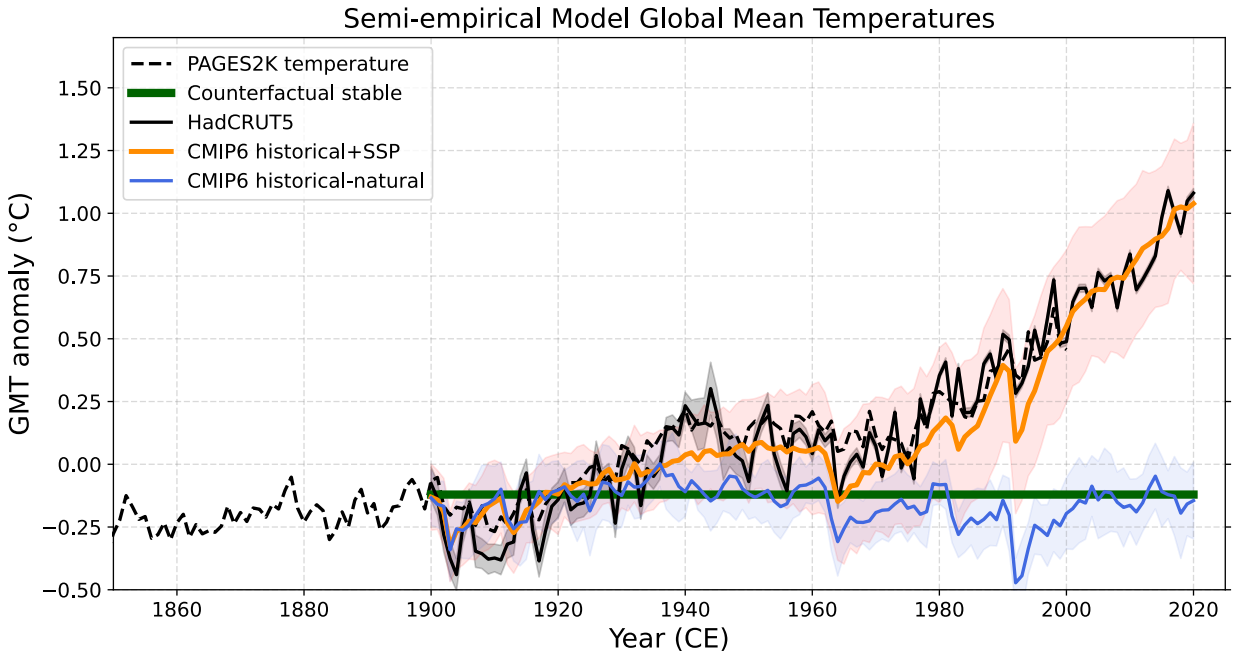

Fig. S1. Global mean temperature anomaly forcings for semi-empirical model runs. Included are the PAGES2K temperature reconstruction over the common era (black dashed line), the Stable counterfactual scenario (bold green line), the observed HadCRUT5 mean and standard deviation temperature (solid black line and shading), the ensemble mean and standard deviation of CMIP6 historical+SSP runs (orange line and shading) and historical natural runs (blue line and shading).

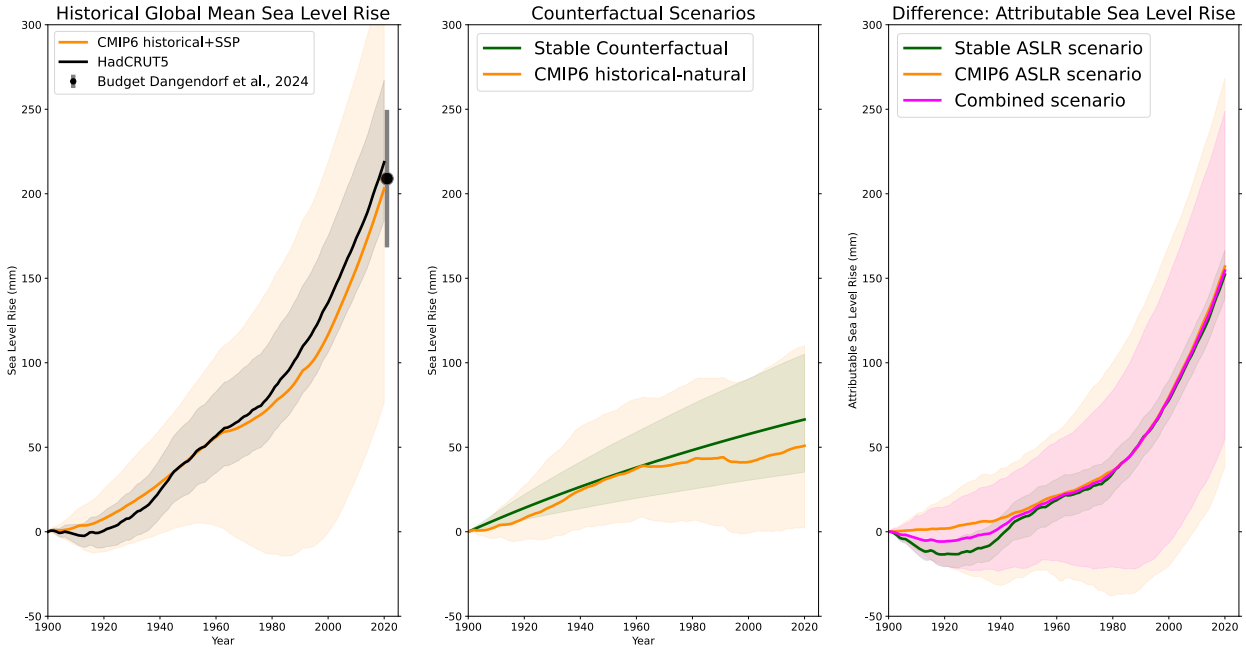

Fig. S2. Historical GMSLR, counterfactual sea levels, and attributable sea level rise from semi-empirical model simulations. Lines and shading are means and ±1σ, respectively. (left) Semi-empirical model estimates of global mean sea level rise associated with the HadCRUT5 historical forcing (black) and CMIP6 historical+SSP forcing (orange). 2018 Estimates from Dangendorf et al. (*66*) are included for comparison. (center) Estimates of GMSL associated with the counterfactual Stable and CMIP6 scenarios. (right) The global mean attributable sea level rise associated with the counterfactual Stable and CMIP6 scenarios—defined as the difference between the historical and counterfactual estimate—and their combined (equally-sampled) distribution (pink curves).

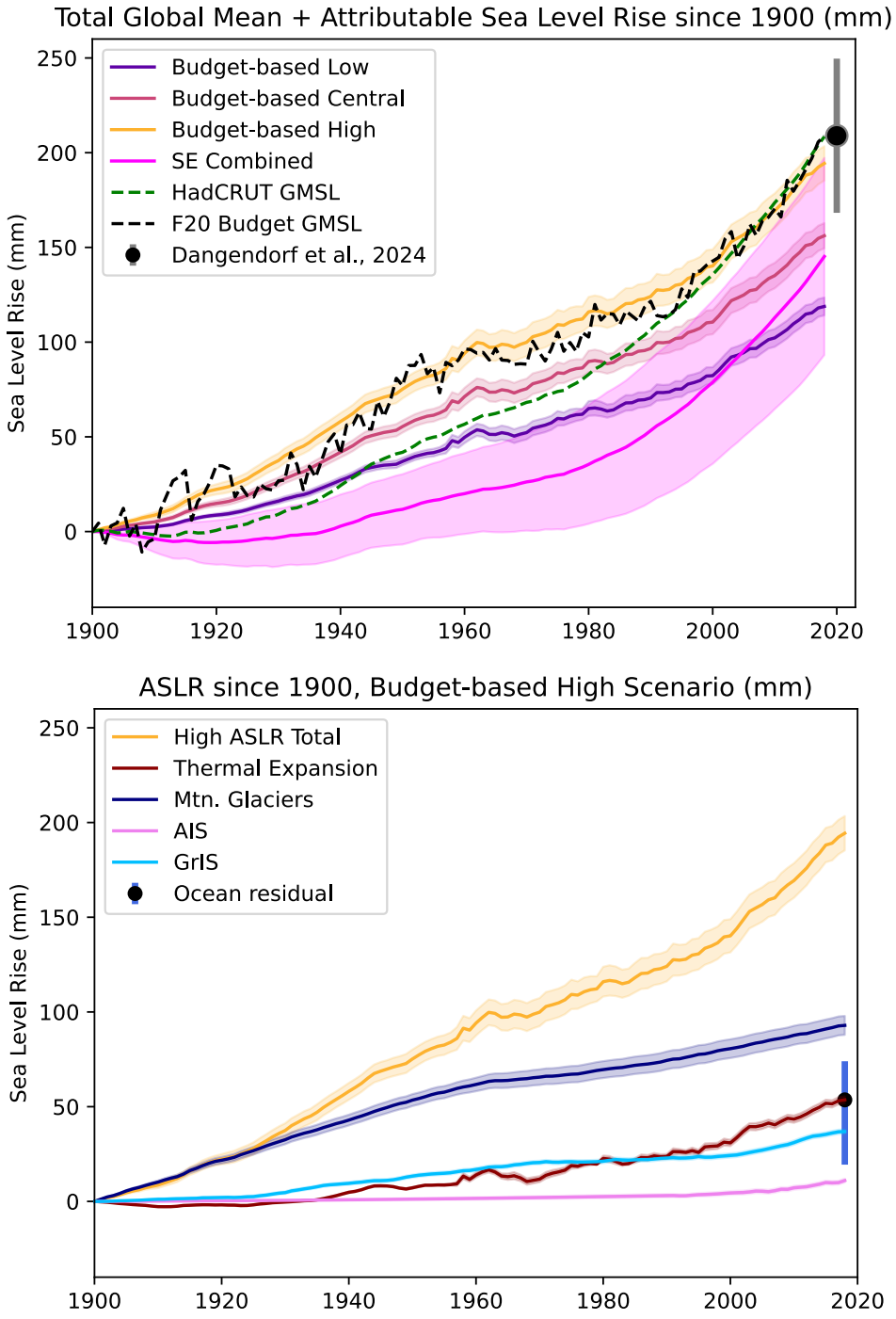

Fig. S3. (top) Timeseries of global mean sea level change and ASLR across various scenarios over 1900–2018. Included are budget-based ASLR, the combined semi-empirical model ASLR, the semi-empirical modeled HadCRUT5 global mean sea level change, the F20 budgeted sea level change, and estimates from ref. *66* for comparison. (bottom) Timeseries of each individual contributing factor to the global budget-based high scenario ASLR. Included is the 95% CI of the regional steric term across tide gauge stations in 2018 (blue bar). Lines and shading are means and ±1σ, respectively.

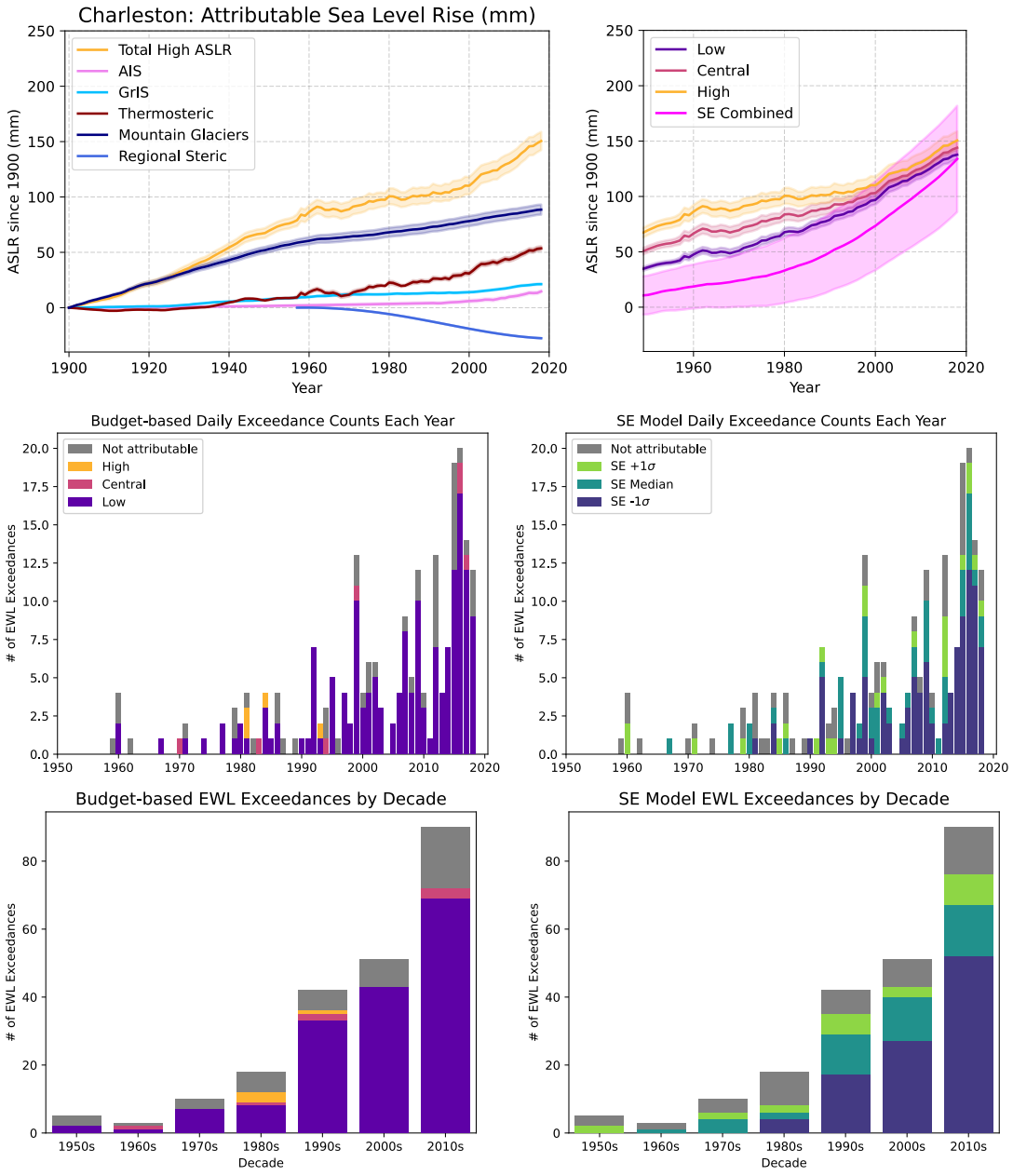

Fig. S4. (top row) Summary timeseries study results at Charleston, SC. Attributable sea level individual contributing budget factors over 1900–2018 and total for the high budget-based scenario (top left), compared with combined (CMIP6 and Stable scenario) semi-empirical model output since 1950 and the low/central budget-based scenarios (top right). Lines and shading are means and ±1σ, respectively. (middle row) Observed annual number of daily exceedances of the 2σ daily highest tide that were not attributable (grey bars) and exceedances that were attributable based on removal of each of high, central, and low budget-based counterfactual sea levels (middle left) and semi-empirical mode scenario counterfactual sea levels (middle right) from the local sea levels. (bottom row) Cumulative number of attributable and non-attributable exceedances per decade, observed or estimated attributable under each budget-based or semi-empirical model counterfactual.

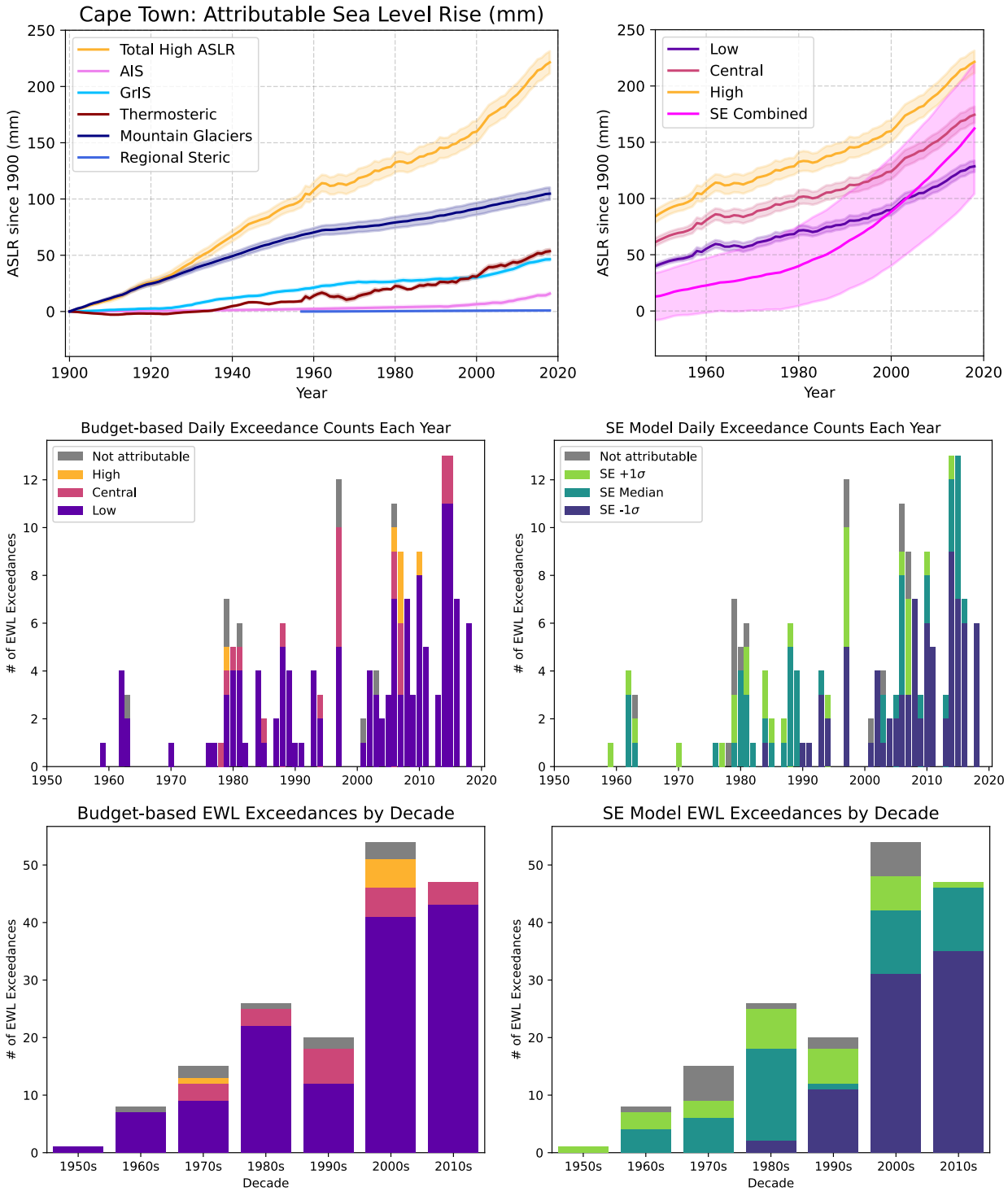

Fig. S5. As in Fig. S4 but for Cape Town.

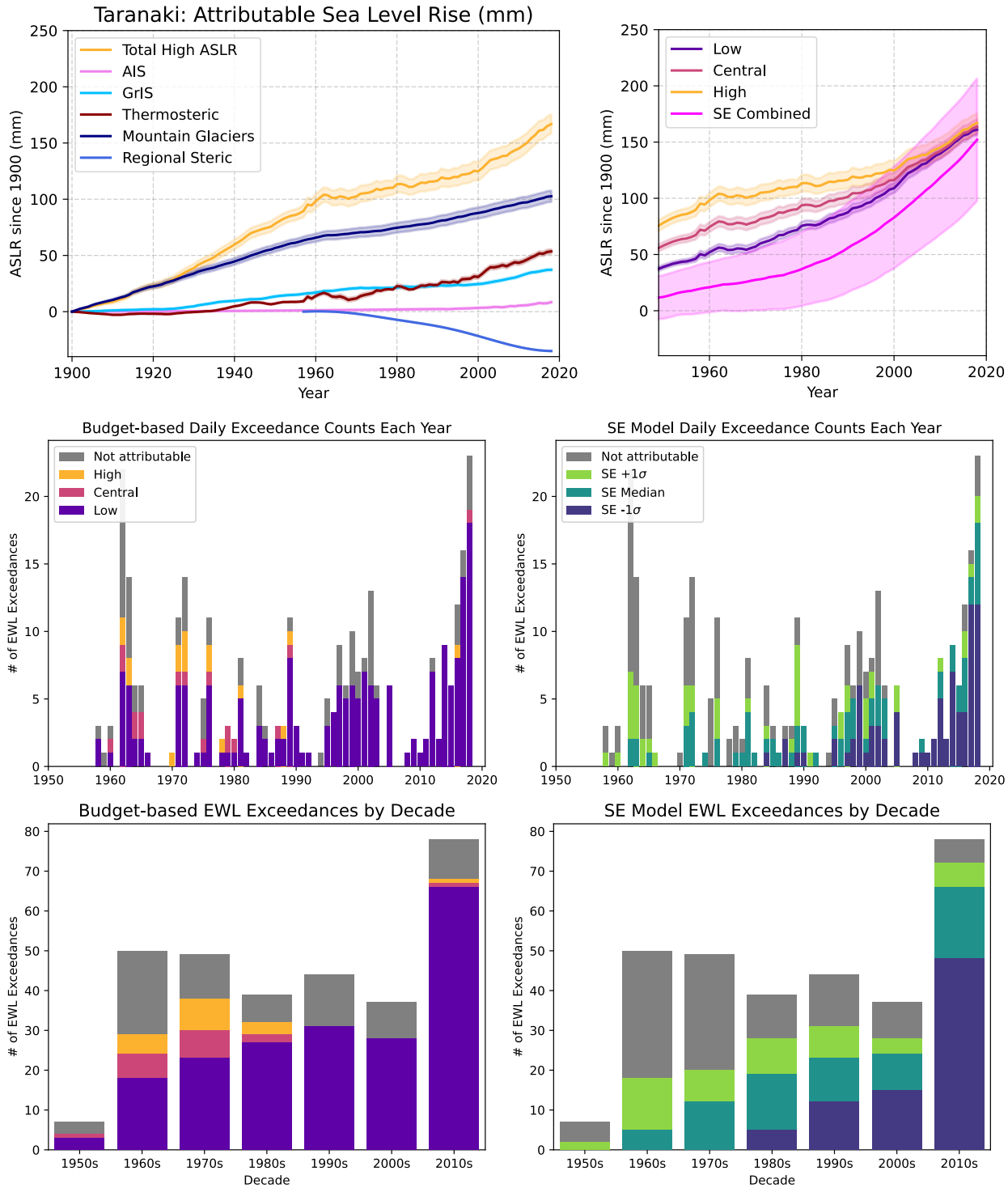

Fig. S6. As in Fig. S4 but for Taranaki, NZ.

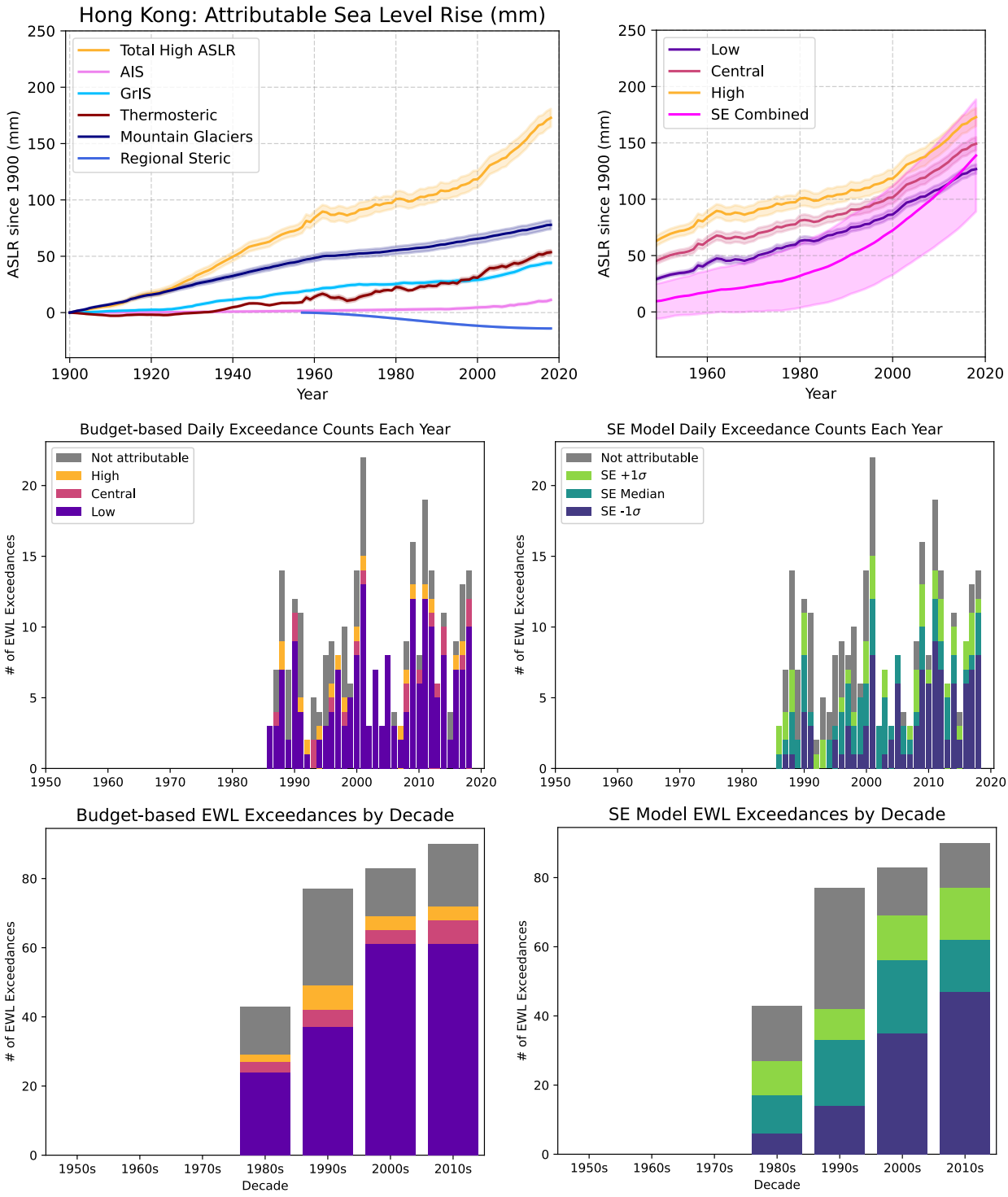

Fig. S7. As in Fig. S4 but for Hong Kong.

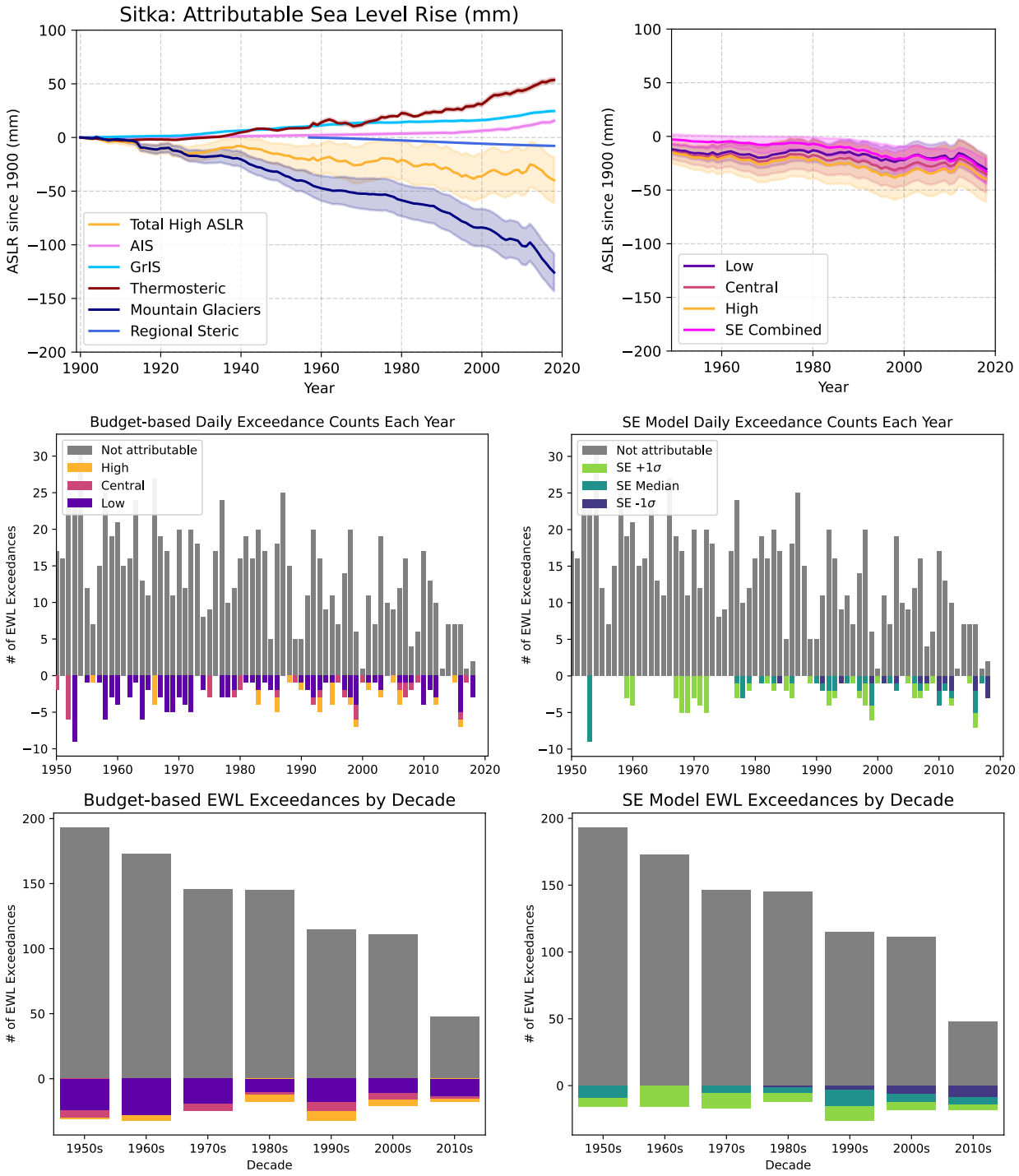

Fig. S8. As in Fig. S4 but for Sitka, AK.

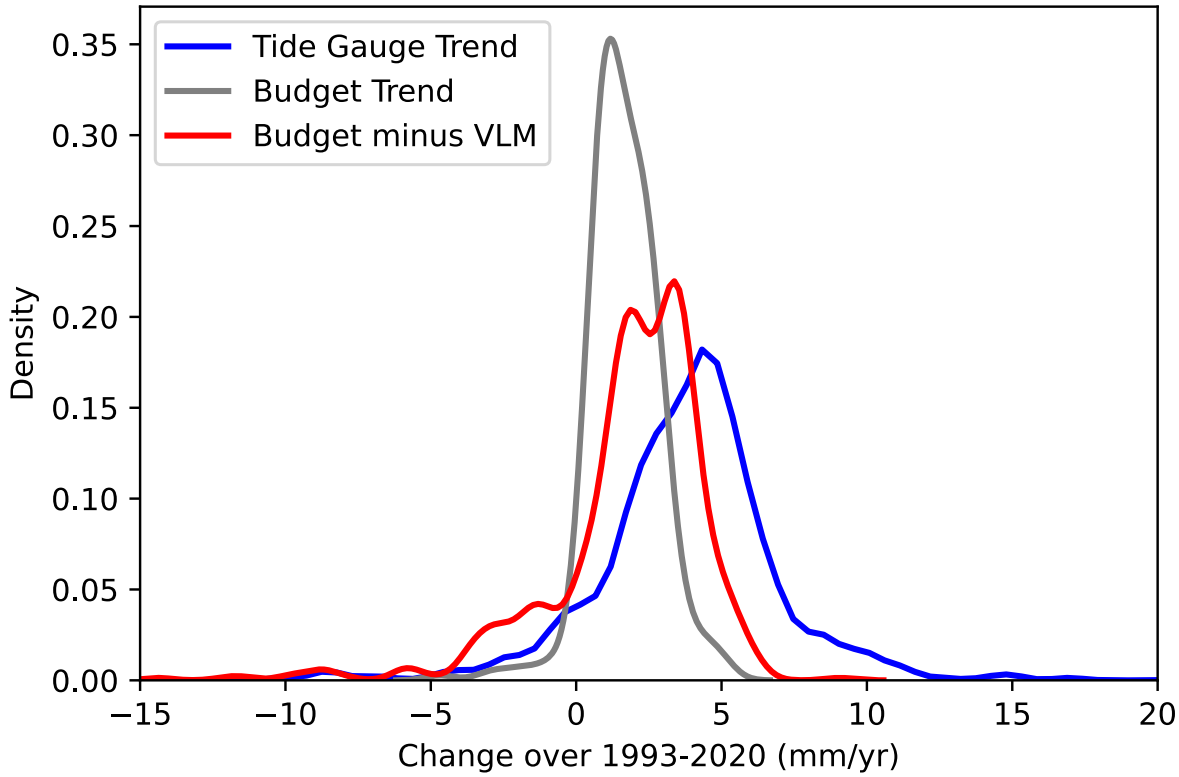

Fig. S9. Probability Density Functions over GESLA stations in this study of observed sea level trends (blue curve), budget trends (grey curve), and budget trends minus vertical land motion (red curve); all in mm/yr over 1993–2018/20.

5

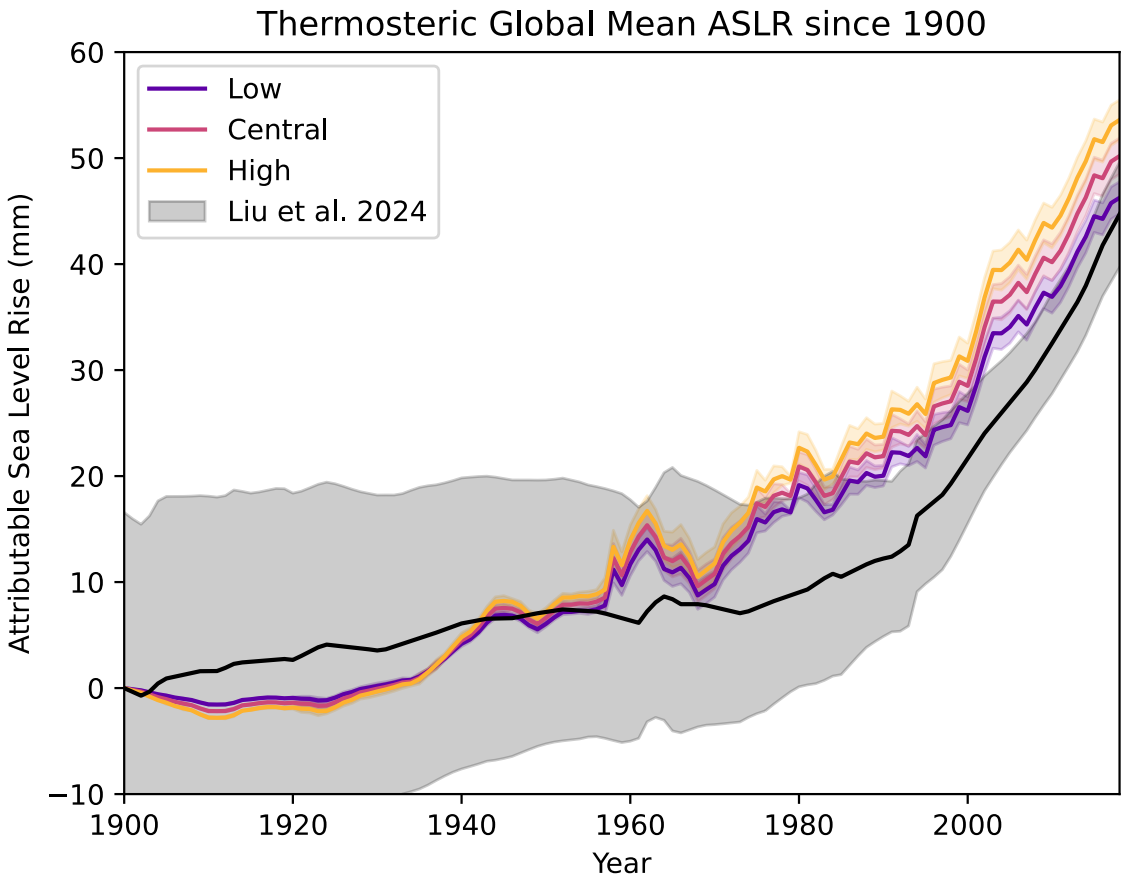

Fig. S10. Thermosteric sea level rise since 1900 estimated from our low, central, and high budget-based counterfactuals compared with estimates from ref. *6*.

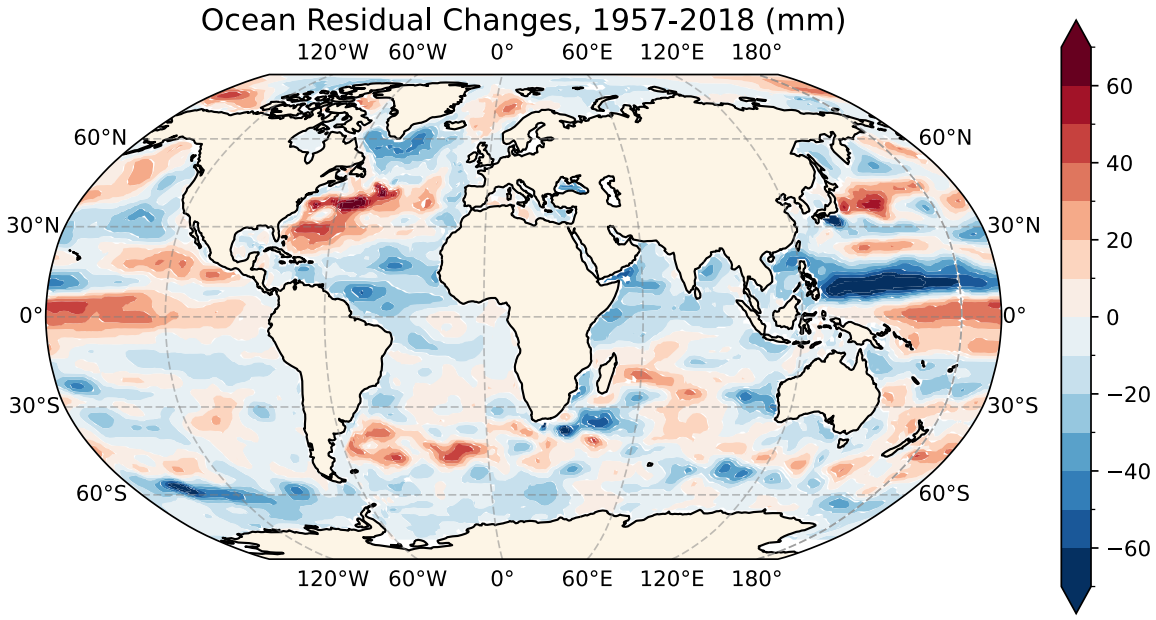

Fig. S11. The total sea level change in the ocean regional steric term over 1957–2018.

5

Table S1.

Semi-empirical sea level model parameters, priors, and posterior estimates. τ indicates the timescale on which the actual temperature relaxes toward the equilibrium temperature, and τ_c is e-folding time for temperature independent term *c*. Relative to K16 (*24*), the new posterior distributions were sampled using new global mean sea level and global mean surface temperature estimates from ref. *13* and *24*, respectively. Ranges shown for posteriors are 5th–95th percentiles. Temperatures are relative to the 1850–2000 CE average.

Parameter	Prior	K16	This Study
a	U(0, 20) mm/yr/K	4.0 (3.2, 5.4)	4.93 (4.40, 5.55)
c (500 CE)	U(-10, 10) mm/yr	0.22 (0.10, 0.42)	0.25 (0.16, 0.36)
c (2000 CE)	U(-2, 2) mm/yr	0.14 (0.05, 0.29)	0.14 (0.07, 0.23)
T_0 (-2000 CE)	U(-0.22, 1.0) K	0.25 (-0.19, 0.89)	0.16 (-0.37, 0.72)
T_0 (500 CE)	N(0.12, 0.2) K^2	0.17 (0.11, 0.23)	-0.02 (-0.07, 0.05)
T_0 (2000 CE)		-0.05 (-0.12, 0.07)	-0.07 (-0.13, 0.02)
τ	log U(30, 3000) yrs	174 (87, 366)	130 (90, 181)
τ_c	log U(1000, 20000) yrs	4175 (1140, 17670)	7785 (1676, 20000)